

Chapter 3

The Photothermal Effect

The purpose of the experiments described in this chapter is to measure how light intensity fluctuations in a Fabry-Perot cavity can cause length changes in the cavity. The dominant mechanism for this is believed to be the photothermal effect.

3.1 Introduction

The photothermal effect as a source of noise for LIGO was introduced by Braginsky, Gorodetsky, and Vyatchanin (BGV99) [22], who observed that shot noise fluctuations in the interferometers' laser power could drive surface fluctuations in the test masses. The way this is believed to happen is that the test masses' dielectric mirror coatings absorb a small amount of light power, converting it to heat, which diffuses through the mirror. The theory for photothermal noise in a test mass substrate (see §2.4.1) was worked out by BGV99 and Cerdonio *et al.* [32], assuming that the laser spot is much smaller than the mirror dimensions and that the absorption of light and conversion to heat takes place in a thin layer at the mirror surface.

De Rosa *et al.* [106] have observed this effect with two Fabry-Perot interferometers made from four identical fused silica mirrors, when they varied the power to one cavity and measure its length change relative to the other. Their measurements agreed well with the theory for homogenous substrates from 10 mHz to 200 Hz, but they did not address contributions from the mirror coatings.

I will discuss the design of an instrument that measures an interferometer's response to heat fluctuations at the surface of a mirror and how the response changes in the presence of a dielectric coating. This instrument is built around a cross-polarized Fabry-Perot interferometer, in which two beams of orthogonal polarization resonate simultaneously in the same cavity. One of the cavity's mirrors is a standard high-reflectivity interferometer mirror. The other, the "test" mirror, is a

specially made mirror with a medium absorption (1-3%) metal surface. One of the laser beams is intensity-modulated to alternately heat and cool the test mirror, while the other beam measures the motion of the surface of the test mirror. In order for the theories of BGV99 and Cerdonio *et al.* to apply to these measurements, it is necessary that spatial profiles of both beams overlap on the test mirror. Since these experiments are conducted with a Fabry-Perot cavity, this condition is automatically satisfied if both beams simultaneously resonate in the TEM₀₀ mode of the interferometer.

The photothermal effect is often used (particularly in the semiconductor industry) to measure thermal properties of materials [67, 9]. A common configuration is the modulated photothermal deflection experiment [83, 10], in which a “pump” laser beam, chopped into a square wave, strikes a sample at normal incidence, while a “probe” beam strikes the sample at a glancing angle. The pump beam is partially absorbed by the sample, raising a blister, which is observed by an angular deflection of the probe beam. A variation on this method uses the sample as one arm in a Michelson interferometer, with a displacement sensitivity of 4×10^{-13} m, limited by the pointing and intensity fluctuations of the probe beam [95]. While well developed, these methods are not optimal for measuring the photothermal effect in the mirrors that LIGO uses, as they work best on materials with highly absorptive surfaces. A new way to measure the photothermal response of a highly reflective sample is to use a Fabry-Perot cavity to recycle the pump beam power. This way, optical power that would otherwise be wasted can build up in the cavity until it is absorbed by the sample. Major advantages of this new technique over traditional photothermal methods are that it is more sensitive, only requires one laser, and has a large dynamic range. It can take measurements at audio frequencies above 5 Hz, with the sample displacement ranging from 4×10^{-15} m to 10^{-9} m on a tabletop.

This chapter presents measurements of the photothermal response of several mirrors, whose preparations are described in §3.2.6. The first measurement was done with a solid aluminum mirror, whose behavior is compared with the homogenous solid theory [32] from 10 Hz - 4 kHz. Since recent measurements [5, 20, 30, 56, 118, 127] suggest that the thermal expansion coefficient of thin films used by LIGO could be on the order of 2×10^{-6} /K, several times higher than for bulk silica [35], I examined BK7, fused silica, and sapphire substrates, each with mirrored and unmirrored samples. The samples were used to find whether the mirror coating has a substantial effect on the photothermal response. In order to give these samples similar reflective surfaces without strongly influencing heat flow, these samples all have a thin ($\sim 1.8 \times 10^{-7}$ m) layer of gold evaporated on them.

To summarize, the samples tested are

- Solid aluminum
- Gold-coated fused silica
- Gold-coated fused silica with a 30-layer HR mirror ($\text{TiO}_2/\text{SiO}_2$)
- Gold-coated BK7
- Gold-coated BK7 with a 30-layer HR mirror ($\text{TiO}_2/\text{SiO}_2$)
- Gold-coated c-axis sapphire
- Gold-coated c-axis sapphire with a 30-layer HR mirror ($\text{TiO}_2/\text{SiO}_2$)

3.2 Materials and Methods

A laser beam is split into two cross-polarized beams, denoted *pump* and *probe*, then recombined and resonated together in a Fabry-Perot interferometer (IFO). The *pump* beam is used to modulate the light power that strikes the test mirror, while the *probe* beam detects length changes in the interferometer with the Pound-Drever-Hall (PDH) [43, 41] optical heterodyne technique and also locks the laser frequency to the cavity resonant frequency. The *pump* beam is periodically interrupted with a chopping wheel, converting it to a pulsed beam with a 50% duty cycle. Analyzing the length changes at the chopping frequency comprises a direct, lock-in measurement of the photothermal effect, as the PDH signal represents the average displacement of the test mirror surface, weighted by the Gaussian beam profile [82, 22].

The greatest challenge in building this instrument is in reducing cross-coupling between the reflected *probe* and *pump* beams. The purpose of the highly redundant polarizing optics is to minimize the amount of *pump* light reflected back along the *probe* path. In implementing this device, I used two designs to counteract cross-coupling: a preliminary layout sufficient for measuring the photothermal response in aluminum, and a more complicated layout with better mode matching and more polarizing optics to reduce cross-coupling noise for the other samples.

3.2.0.1 Aluminum measurements

To construct the instrument (Fig. 3.1), I divide the beam from a laser (§3.2.5) into the *pump* and *probe* beams with a polarizing beamsplitter (PBS) (7). A half-wave plate (6) determines the power

diverted by a Faraday rotator (19) and a PBS (18) to the RF photodiode (RFPD). The output of the RFPD is demodulated according to the PDH method, giving the signal that measures changes in the cavity length. The PDH signal is also used with a feedback servo (27) (see §3.2.4) to keep the laser resonant with the IFO.

For the aluminum measurement, the interferometer finesse² is only 37, so mode matching and alignment requirements are not very strenuous. Lenses (1, 5, 23) and steering optics on kinematic mounts (4, 6, 11) focus and align the beams for injection into the interferometer.

Faraday isolators (2, 9, 14) prevent reflected beams from feeding back to the laser. Without the isolators in the *pump* and *probe* beams (9,14), spurious reflections in the first PBS (7) can cause a fraction of the *pump* light reflected from the cavity to travel through the EOM, reflect from the cavity, and finally reach the RF photodiode, creating cross-coupling noise. These and extra PBSs (8, 21, 17) and a plane polarizer (PP) (28) reduce the amount of *pump* light that reaches the RFPD. Half-wave plates (3, 6, 12, 15, 20) rotate beam polarizations to compensate for rotations by Faraday isolators (2, 9, 14) and rotators (19), misalignments between PBSs, and to place the beam in horizontal or vertical polarizations before reflection or transmission through any optics.

The IFO is made from two mirrors held 31.8 cm apart by an aluminum spacer block. The input mirror (24) is a concave fused silica substrate with a low absorption dielectric mirror coating, a reflectivity of 95%, and a radius of curvature of 50 cm. The “test” mirror (25) is mounted at the other end of the interferometer cavity (see §3.2.5.5). The test mirror has an absorptivity of around 6%, while the input mirror’s absorptivity is much less. Since the photothermal effect scales linearly with the amount of power absorbed, and depends on absorption, IFO length changes due to the photothermal effect will be dominated by the test mirror. The absorption of the test mirror is determined by fitting its measured photothermal response to Eq. 2.26.

A drawback with this configuration is that the beam does not couple well into the cavity. Since cross-coupling noise depends on the amount of power reflected from the cavity, I chose to improve the mode matching, which imposed constraints (see §3.2.1) that forced changes to the optics layout.

3.2.0.2 BK7, Fused Silica, Sapphire

In this version of the instrument, the beam makes several changes between horizontal (H), vertical (V), and mixed (M) polarizations as it travels around the optics table. H-polarized light passes

in only one direction.

²Finesse is a measure of the optical gain of a cavity. See §5.3.

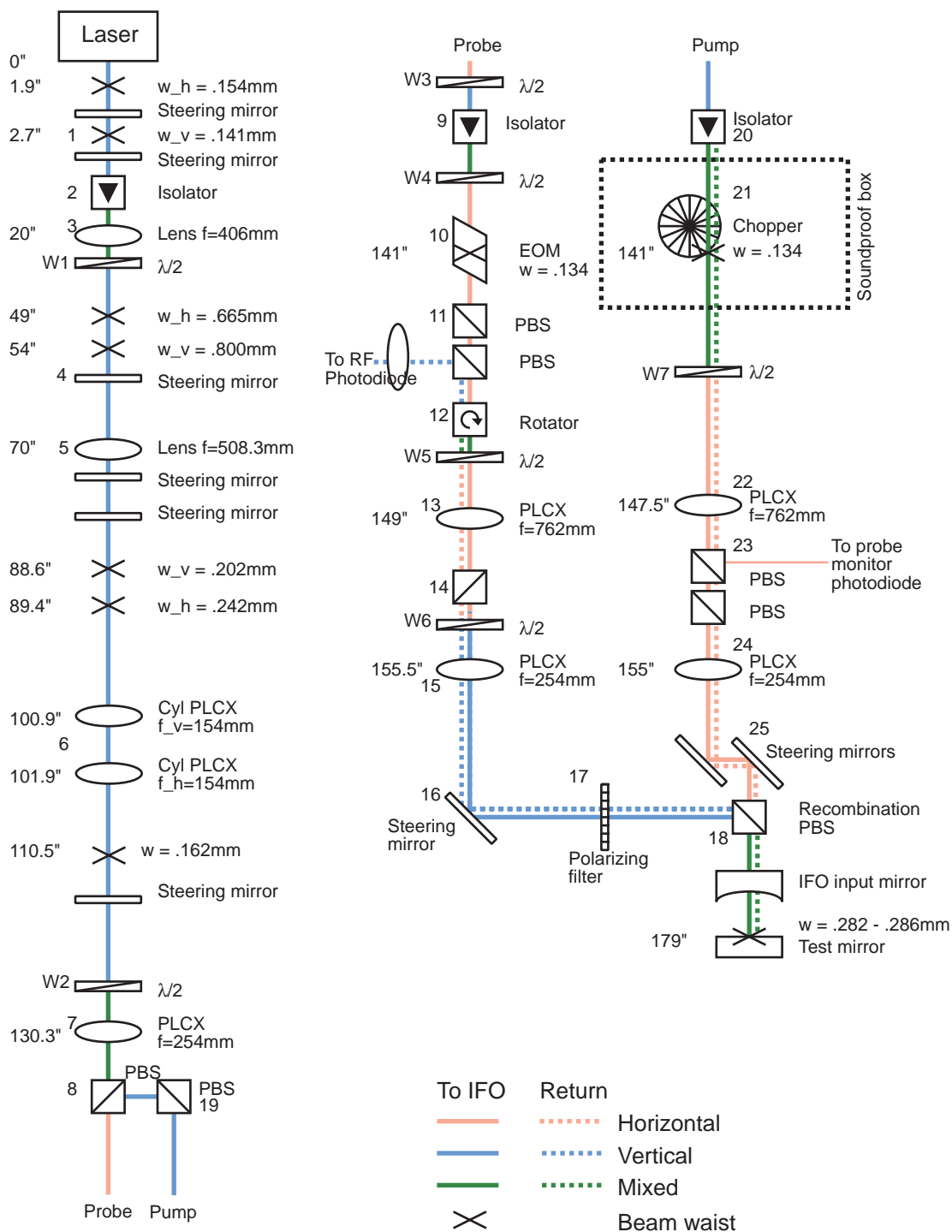


Figure 3.2: Linearized view of the experiment layout for BK7, fused silica, and sapphire. Shaded lines represent laser beams, and solid black lines represent wires. Black x's represent beam waists. Waist radii are measured in $1/e$ of field amplitude, in accordance with the formalism of Kogelnik and Li [77].

directly through polarizing beamsplitter (PBS) cubes, while V-polarized light is reflected. Mixed polarization occurs after Faraday optics or when H- and V-polarized beams are combined. To make a circular beam spot that couples well to the cavity requires a long optical path (see §3.2.1). Fig. 3.2 shows the unwound optical layout, with the beam waists³ marked. Details of the mode-matching procedure are given in §3.2.1.

Starting at the laser, the elliptical, V polarized beam travels through a short periscope (1) and through a Faraday isolator (2). The periscope is used to find a “sweet spot” with minimum distortion by the isolator. Now with M polarization, a lens (3) refocuses the beam to form large, elliptical waists at around 50”. A half-wave plate rotates the beam’s polarization to restore vertical polarization before a 90° turn at a steering mirror (4). These mirrors (New Focus 5014 or CVI Y1-1025-UNP-FG) are birefringent, and can convert a beam with linear M polarization into one with partial circular polarization⁴, so it is important to put the light into either H or V polarization with a half-wave plate (W1) before changing its direction.

Another lens (5) focuses the beam to form a waist as the beam reaches the end of the table and returns back. Two cylindrical lenses (6), oriented horizontally and vertically, focus the beam to a single circular waist at 110.5” before the beam takes another 90° turn. A half-wave (W2) plate selects the power distribution between the *probe* and *pump* beams before the beam passes through another mode-matching lens (7). The beam is split into *probe* and *pump* arms by a polarizing beamsplitter (8).

In the *probe* path, a half-wave plate restores vertical polarization for the light to pass through another isolator (9). Another half-wave plate rotates the beam to horizontal polarization for the electro-optic modulator (EOM) (10), which is also birefringent. The EOM is positioned about a tight beam waist, to minimize clipping at its narrow apertures. To make sure the beam is purely H-polarized, it passes through two more PBSs (11). Each beamsplitter has an extinction ratio of 1000 : 1 [36], and with good alignment, their collective extinction ratio⁵ is improved to about 10⁵ : 1.

After this polarization filter, the *probe* beam goes through a Faraday rotator, which is just an isolator without its polarizing filters. A half-wave plate brings the beam back to H polarization

³Laser beams can be focused to a minimum spot size, called a beam waist. They expand symmetrically on both sides of the beam waists with a hyperbolic profile [77].

⁴Determined by reflecting a $\frac{H+V}{\sqrt{2}}$ beam off a steering mirror at 45°, and measuring the power transmitted and reflected by the second of two polarizing beamsplitter cubes.

⁵Determined by measuring the reflected power when V-polarized light (which should not be transmitted) is shone through a pair of beamsplitters.

so that it will pass straight through another PBS (14). Then, another half-wave plate rotates the beam to V polarization so that it will reflect at the recombination PBS (18). A compound mode-matching telescope (13, 15) images the final beam waist at the surface of the test mirror. A linear glass polarizer (17) on a precision rotary mount is critical for removing H-polarized light from the reflected beam. The steering mirror (16) and final PBS form the steering periscope for the *probe* beam.

Upon reflection from the cavity, the *probe* beam returns along its path until the Faraday rotator (12). There, it is shifted to V polarization, and is bent out of the main beam path by the next beamsplitter, where a cat's eye lens⁶ focuses it onto the RFPD.

From the start of the *pump* path at (18), a PBS (19) takes the beam through a 90° turn into a Faraday isolator (20). The chopper wheel (see §3.2.5.4) intersects the beam at a small waist to help reduce systematic phase noise (see §3.2.7.6). The beam is then rotated to H polarization, and passes through a mode-matching telescope (22, 24) and polarization filter (23) before recombining with the *probe* beam at a PBS (18). A neutral-density filter may be placed before the alignment periscope (25) to attenuate the *pump* beam. Upon reflection from the cavity, the *pump* beam returns along its path until it is arrested by a beam dump at the Faraday isolator (20).

With the polarizing optics (see §3.2.2) set correctly, it is possible to reduce the power from the *pump* beam reaching the RFPD to 10^{-5} of that impinging upon the cavity. This is measured continuously as part of the data acquisition process to characterize the cross-coupling noise.

3.2.1 Mode matching

The laser spot size ($1/e$ of field amplitude) at the test mirror is 0.28 mm, determined by the length of the cavity and the curvature of the input mirror. Spot sizes used for mode matching calculations refer to the radius w at $1/e$ of the central field amplitude, so that $w = \sqrt{2}r_0$, where r_0 is the spot size as used in Chapter 2 and in much of the thermal noise literature. The TEM₀₀ resonant axis of the IFO is determined by the line normal to the surface of the test mirror that passes through the center of curvature of the input mirror; with both *pump* and *probe* beams optimally aligned to the cavity, they are collinear in the cavity and the *pump* beam heats the same spot that the *probe* beam senses.

The mode matching was calculated with a spreadsheet⁷ [103] using the formalism of Kogelnik

⁶The lens's focal point is at the RFPD.

⁷Included with the online version of this thesis, available at <http://library.caltech.edu/etd/>

and Li [77]. The beam waists indicated on Fig. 3.2 reflect measurements made with a Photon, Inc. dual-axis beam scanner (www.photon-inc.com).

The purpose of the lenses in this instrument is to convert the elliptical beam emanating from the laser into a circular spot matched to the IFO, 179" from the front of the laser enclosure. The Faraday isolator (2) immediately after the laser distorts the beam, so the initial beam waists are not useful for the mode matching calculations. Therefore, the first lens (3) was chosen to produce well-defined Gaussian beam waists at around 50" from the laser, which were taken as the starting point in the beam propagation equations. The next lens (5) was chosen to produce a nearly circular beam, with horizontal and vertical waists displaced by less than an inch (at 89"). This is necessary to allow two cylindrical lenses (6) to image a single circular waist at 110.5". The mounting hardware I used required the cylindrical lenses to be at least an inch apart, so an iterative optimization procedure was used to position the lens (5) so that a solution would be possible. After this circular waist, the beam propagates until another lens (7), whose purpose is to image a waist at the chopper wheel and the EOM.

Having a beam waist at the chopper helps the *pump* beam's amplitude modulation have a duty cycle near 50%, and having a beam waist at the EOM reduces clipping at the EOM's narrow apertures. Each of the arms have a mode matching telescope (13 and 15 in *probe*, 22 and 24 in *pump*) to focus the beam to a waist at the test mirror. The positions of these mirrors are initially determined by calculations with the spreadsheet, then adjusted on the table to minimize the interferometer's reflectivity on resonance.

A critical constraint is that there be 30" to accommodate optics and mounting hardware between the lens (7) and the input mirror of the cavity, with minimal optics between the last lenses (15,24) and the cavity.

3.2.2 Polarization optics

Cross-coupling noise in this experiment is like any other scattered light phenomenon [102]: a stray beam at the carrier frequency but with a random phase beats against the sidebands to make a spurious PDH signal. The technique for measuring the cross-coupling is simple: with the *probe* beam blocked immediately after the first PBS, measure the amount of light that reaches the RFPD.

I have developed the following procedure for optimizing the polarizing optics:

1. Turn off all the room lights except for one. This will make it easier to use IR viewer cards.

2. Place a PBS immediately after the first waveplate (W1), and rotate W1 to minimize the light transmitted by the PBS. Remove the PBS.
3. Set W2 so that the *probe* beam has twice as much power as the *pump* beam.
4. Replace W4 with a power meter. Rotate W3 to maximize the power transmitted by the isolator (9).
5. Replace the PBSs (11) with a beam scanner, and adjust the tip/tilt of the EOM to minimize beam distortion.
6. Restore W4 and PBSs (11) and minimize the power reflected to the side by the PBSs.
7. Remove W5 and use the beam scanner at PBS (14) to minimize beam distortion from the Faraday rotator (12).
8. Restore W5 and rotate it to minimize the power reflected to the side by the PBS (14).
9. Block the *probe* beam at W3 and restore the *pump* beam. Rotate W7 to minimize the light deflected by the PBS (23).
10. With *probe* still blocked, restore the polarizing filter (17) and rotate it to minimize the light transmitted back through it.
11. Restore the *probe* beam and rotate W6 to maximize the power reaching the cavity.

3.2.3 Alignment

Since the test mirror is opaque⁸, I have developed the following procedure to align the lasers to the cavity:

1. Attach the test mirror to the end of the spacer block, with no input mirror. With a 2-mirror horizontal periscope, manipulate the *probe* beam so that it passes through the center of the spacer input aperture and reflects back on itself.
2. Attach the input mirror to the other end. With an IR-sensitive video camera, look through the top of the spacer for a constellation of spots on the end mirror. Scan the beam with the periscope until one appears, and then minimize the scatter of the cluster. The beam should still pass through a spot near the center of the input mirror.

⁸The gold-coated blank substrates transmit a few microwatts of power when the laser is resonant with the cavity.

3. Break a microscope slide cover slip in half. Shine a red laser pointer at it to make sure that it doesn't form an etalon. If it does, you will only be able to see a TEM_{01} mode in the IFO.
4. Turn off the room lights so they don't saturate your cameras.
5. Mount the cover slip inside the cavity at a 45° angle to the horizontal, so that it deflects light upwards into your video camera.
6. Set up a function generator to drive the laser PZT input with a 10Vpp sine wave at 13 Hz (or another frequency relatively prime to 30Hz). Watching the video monitor, manipulate the periscope to make the beam spot symmetric.
7. Setup up photodiodes to monitor the power returned from the cavity and the power inside the cavity. Pointing a photodiode at the test mirror works well. Set up an oscilloscope to trigger on the PZT input and view the photodiode
8. Turn the laser temperature dial until a round TEM_{00} spot is visible (this occurs at a slightly higher laser temperature than the TEM_{01} mode).
9. Without changing its angle, translate the beam horizontally and vertically to maximize the power inside the cavity. You'll need to put the clear cover on top of the cavity to keep the cover slip from blowing around.
10. Remove the cover slip, and again maximize the power inside. This should also minimize the reflected power on resonance. If the input and test mirrors have the same reflectivity, you should be able to reach at least 90% visibility in the carrier. If the test mirror is an "unmirrored" sample, the cavity will transmit a few μW , which a CCD can detect if you turn off the room lights.
11. Place a frequency-doubling viewer disk in front of the cavity, and align the *pump* beam to the *probe*. It helps to set the chopper at a few Hz.
12. Position a photodiode at the *pump* isolator's beam dump (20) to measure the *pump* visibility. Manipulate the *pump* alignment to maximize its throughput. You shouldn't need to use the cover slip for this.

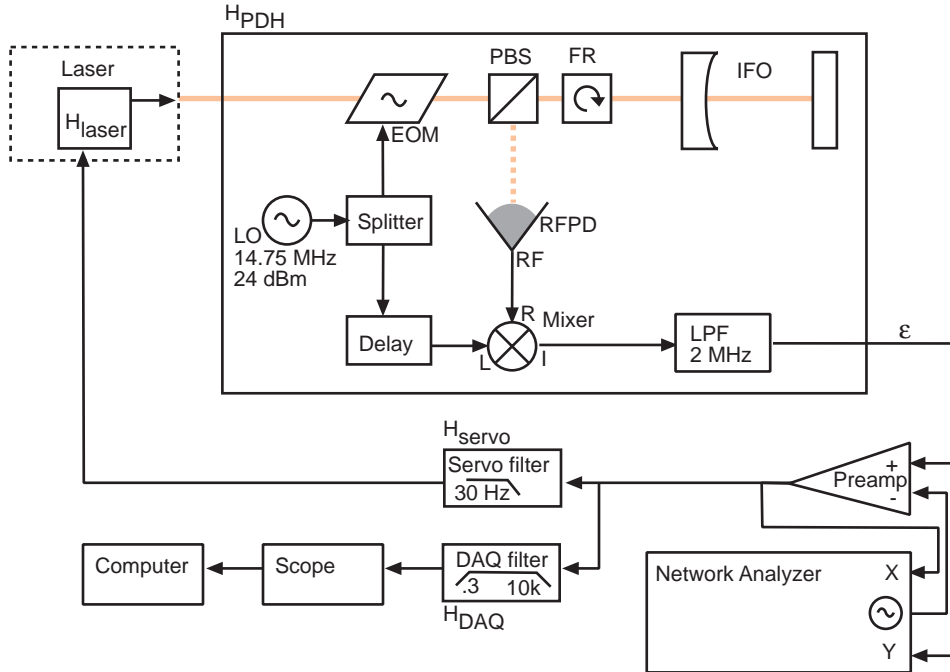


Figure 3.3: Length sensing and control layout, with streamlined optics. Solid lines represent laser beams travelling to the interferometer, and dashed lines represent beams travelling away from the interferometer.

3.2.4 Length sensing, control, and calibration

A control servo locks the laser to the cavity, following the method in Day [41] (Fig. 3.3). The PDH voltage (ε) represents the difference between the laser frequency and the cavity resonance frequency. The factor converting this voltage to units of length is measured in the calibration process.

To detect the length changes, a local oscillator (LO) produces a 10Vpp, 14.75 MHz sine wave. This signal is split, and fed into a tuned resonant electro-optic modulator (EOM) and, via delay cables, to a mixer. The EOM phase-modulates the beam, adding symmetric sidebands, each with 3% of the total beam power. The mixer uses the LO signal to demodulate the RFPD output, the result of which is fed into an in-line low-pass filter (LPF) to remove high frequency components. The output of the LPF forms the PDH signal.

The PDH signal is buffered with a unity-gain differential preamplifier, and fed back to the laser via a filter, H_{servo} . The servo filter is changed between measurements, but is generally a single-pole low-pass filter with gain chosen so that the overall unity gain frequency is below 200 Hz. For data acquisition, the preamp output is subjected to a filter (H_{DAQ}) to reduce DC drift and antialiasing. Data are measured with a Tektronix 3014 digital oscilloscope and copied to a portable computer

(see §3.2.7).

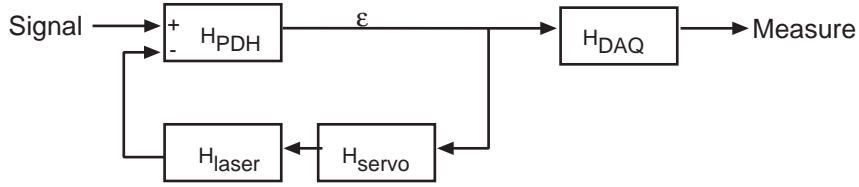


Figure 3.4: Feedback servo block diagram.

The process for determining the PDH response is based on comparing the measured open loop transfer function (OLTF) of the servo to known parameters. First, the OLTF is measured in situ with a network analyzer. With a swept sine signal injected into the preamp, the complex transfer function is

$$OLTF = -\left\langle \frac{Y}{X} \right\rangle = H_{laser} H_{PDH} H_{servo} \quad (3.1)$$

where RF and optical components are treated as a lumped parameter, H_{PDH} . As H_{servo} is known, and H_{laser} is measured independently, measuring the $OLTF$ determines H_{PDH} (see Fig. 3.5). To recover the signal corresponding to the cavity's length changes, we observe (see Fig. 3.4)

$$\begin{aligned} \varepsilon &= H_{PDH}(Signal - H_{laser} \cdot H_{servo} \cdot \varepsilon) \\ Signal &= \varepsilon \left(\frac{1}{H_{PDH}} + H_{laser} \cdot H_{servo} \right) \\ Signal &= \frac{Measure}{H_{DAQ}} \left(\frac{1}{H_{PDH}} + H_{laser} \cdot H_{servo} \right) \end{aligned} \quad (3.2)$$

Both the magnitude and phase of the collected data need to be compensated by this function. With the laser locked and the calibration known, the background noise spectrum is obtained by multiplying the PDH signal by the factor in Eq. 3.2. The dominant source of background noise seems to be acoustic. Therefore, when gathering data, it's important not to talk, listen to the radio, or move around. The cleanroom's laminar flow fans are not the greatest source of noise, and they are necessary to regulate the spacer block's temperature over long timescales. Fig. 3.6 shows a noise curve obtained under ideal operating conditions (after everyone else the building has gone home).

Figure 3.5: Measured open-loop transfer function for the mirrored sapphire measurement, fit with a model for *OLTF*. The data are compensated for the effects of the servo up to 4 kHz. The *OLTF* magnitude at DC is 7.5, the electronic gain is 1, and the DC H_{laser} gain is 6 MHz/V. This sets $H_{PDH} = 1.25V/MHz$. The DC calibration factor for the instrument is therefore $\frac{\lambda L}{c H_{PDH}} = 8.7 \times 10^{-10}$ m/V. With a finesse of 80, the line width is 1.25×10^{-8} m.

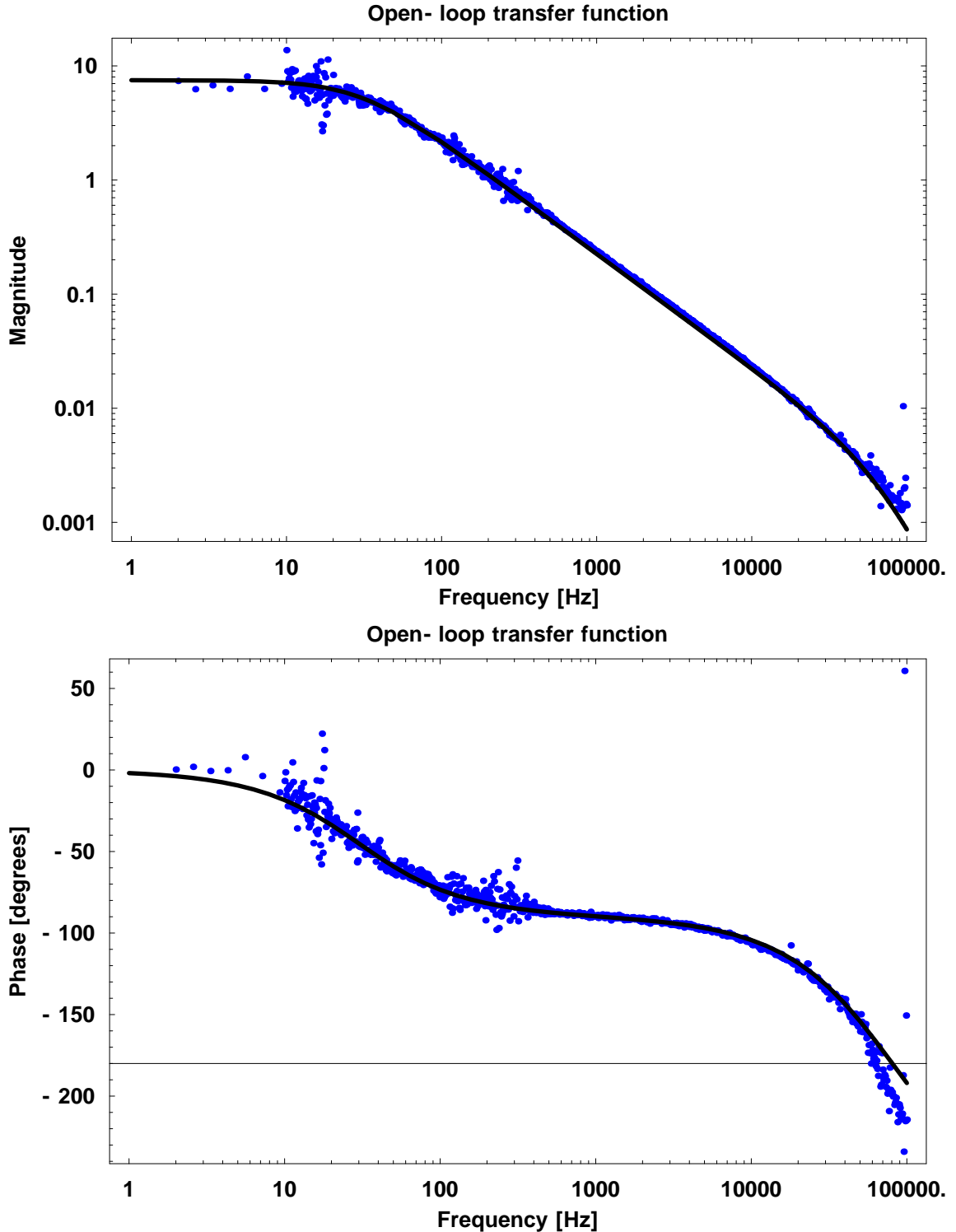
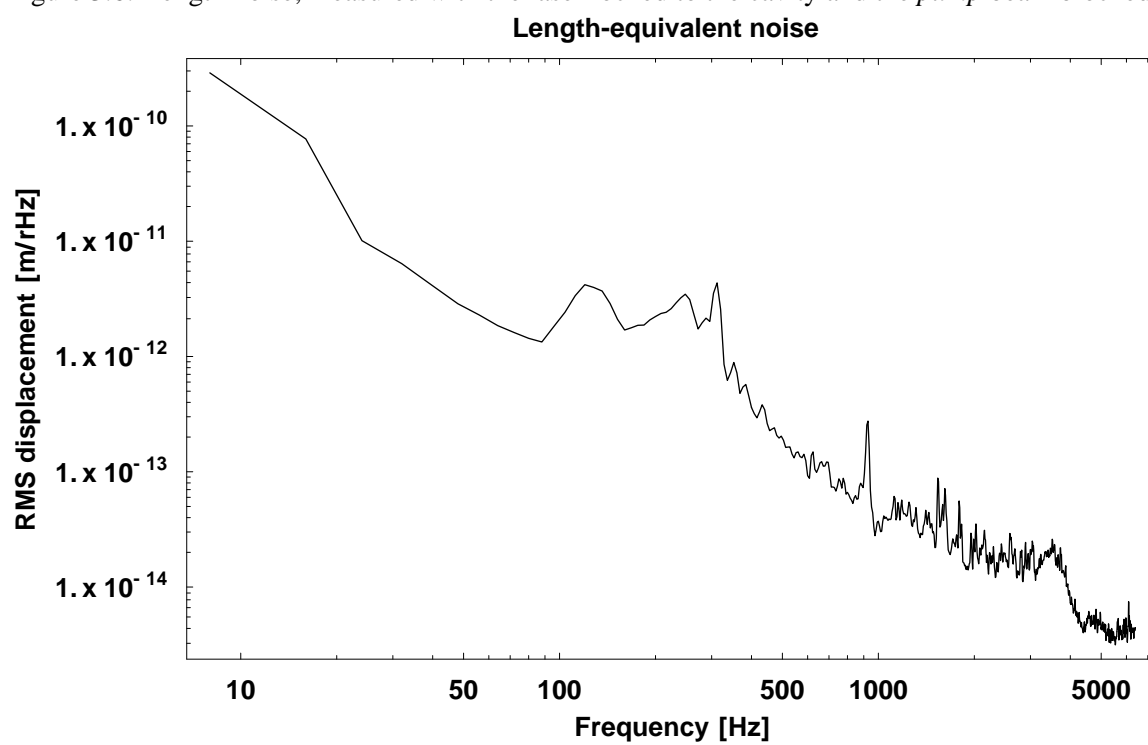


Figure 3.6: Length noise, measured with the laser locked to the cavity and the *pump* beam blocked.



3.2.5 Components

Most of the optics (lenses, mirrors, beam splitters, and wave plates) are stock components purchased from CVI Laser Corp. Part numbers are listed in Table 3.1, and detailed descriptions of the parts follow.

3.2.5.1 Mounting hardware

All the parts used in this experiment lie on a single optical table. Some of them require special mounting hardware.

- Beam splitters are on 3-axis tilt stages, bolted to a steel pedestal clamped to the optical table. The stress from clamping them down tends to induce birefringence, so double-stick tape holds them in place.
- Most of the steering mirrors are held in standard mirror mounts. Those used for alignment to the cavity (16, 25) are held by precision mounts (Lee's Mount replicas). Mirror mounts
- Lenses are mounted in standard 1" \varnothing lens holders, bolted to 1" \varnothing steel pedestals clamped to the table. The pedestals are 2" high with 1/8" stainless steel washers to position the center of the lens 3" above the table surface.
- Non-critical wave plates (W1, W2, W3, W4) are set in standard rotation stages, while the others are set in precision rotation stages with fine-tuning knobs. Rotation stages are bolted to 1" \varnothing steel pedestals, clamped to the table.
- The EOMs and Faraday components are mounted to 4-axis tip/tilt stages. The EOM's mounting hole mates conveniently with these. The Faraday parts are attached to the stages with 5-minute epoxy. The elevation of the tip/tilt stage is set by setting it on a large block of metal of appropriate thickness, while two long 1/4"-20 bolts anchor the stage directly to the table.
- The polarizing filter comes in a custom mounting ring, which is epoxied to a rotation stage.

3.2.5.2 Photodiode

The length sensing and control system is based on a LIGO standard RF photodiode with DC gain of 40V/W. A neutral density filter in front of the RFPD attenuates the light power so that the PDH

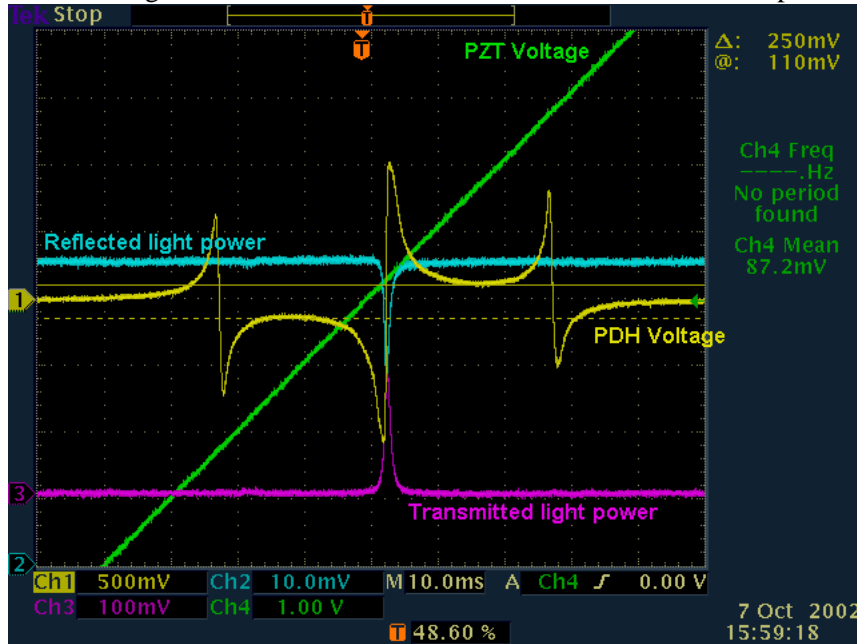
Table 3.1: Optical and electronic components and hardware

| Identifier | Manufacturer | Part number |
|---|----------------------------|-----------------------------------|
| Interferometer input mirror | CVI | PR1-1064-95-1025 |
| Sample: Al | Janos and CVI | see §3.2.6 |
| Samples: BK7, Al ₂ O ₃ , SiO ₂ | CVI | see §3.2.6 |
| Steering mirrors | CVI | Y1-1064-1025-UNP |
| Standard mirror mounts | Thorlabs | KM1 or KM1HC |
| Precision mirror mounts | CVI | PLQ-10 |
| Standard rotation stage | Thorlabs | RSP1 |
| Precision rotation stage | CVI | 1180 |
| Polarizing beamsplitter | CVI | PBS-1064-100 |
| Beamsplitter stage | New Focus | 9411 |
| RF photodiode | LIGO | T980068[86], D980454[112] |
| Faraday rotator and isolators | Electro-Optic Technologies | 1064 μ isolator, 4mm aperture |
| Electro-optic modulator | New Focus | 4003 |
| Tip/tilt stage | New Focus | 9071 |
| Pedestals | CVI | 75-xx |
| Pedestal clamps | CVI | 71 |
| RF Splitter | Mini-Circuits | ZFSC-2-1W |
| RF Mixer | Mini-Circuits | ZAY-3 |
| LPF (Low-Pass Filter) | Mini-Circuits | BLP-1.9 |
| Preamplifier | Stanford Research | SR560 |
| Servo filter | Stanford Research | SR560 |
| DAQ filter | Stanford Research | SR560 |
| Network Analyzer | Stanford Research | SR785 |
| Local RF oscillator | Stanford Research | DS345 |
| Delay | EG & G | BNC cable box |
| Data capture | Tektronix | TDS3014 |

signal stays within its linear range of $2 V_{pp}$. The photodiode's DC response saturates at 100 mW, but its tuned RF amplifier saturates if its output amplitude is more than a few volts.

3.2.5.3 Laser

Figure 3.7: Laser PZT Calibration. The sidebands are separated by 14.75 MHz.



The laser is a 400 mW, 1064 nm, diode-pumped Nd:YAG non-planar ring oscillator (LightWave Electronics Model 126, <http://www.lwecorp.com/>), rigidly mounted to the optical table at a 3" beam height. The laser's power supply allows for controlling the laser frequency by adjusting the temperature and by mechanically stressing the crystal with a PZT. Slow changes over several GHz can be affected with temperature, while fast changes over a few MHz require the PZT.

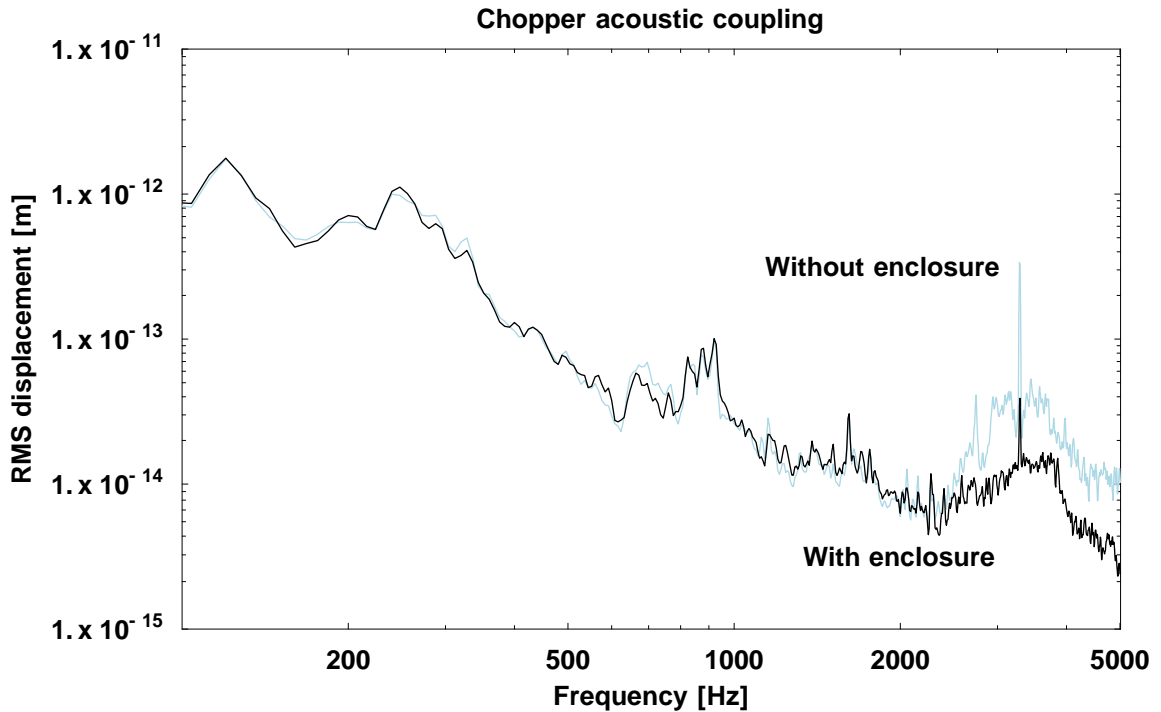
The DC value of the transfer function of the laser PZT, H_{PZT} , is found by measuring the PDH signal for a high-finesse (500) cavity while applying a slow (10 Hz) voltage ramp to the PZT (Fig. 3.7). The beam resonates in the IFO at three frequencies corresponding to the carrier and two sidebands, each 14.75 MHz away from the carrier frequency. The calibration factor is simply $\frac{2 \times 14.75 \text{ MHz}}{\Delta V}$.

The PZT also has a high frequency pole, which is determined from the servo transfer function (see §3.2.4). In 2000, the H_{PZT} was measured to be 6.3 (MHz/V) with a pole at 55kHz. By 2003, the DC gain had degraded to 6.0 (MHz/V). For all the data reported here, the DC PZT gain is 6 MHz/V. The PZT appears to have a single pole at 55 kHz for the Aluminum mirror experiments,

which were done in mid-2002. By 2003, when the other materials were measured, the PZT pole decreased to around 32 kHz, possibly from failure of the bond between the PZT and the laser crystal.

3.2.5.4 Chopper

Figure 3.8: Effectiveness of the acoustic isolation box around the chopper wheel. Light blue: rms length noise without the box. Black: rms length noise with the box.



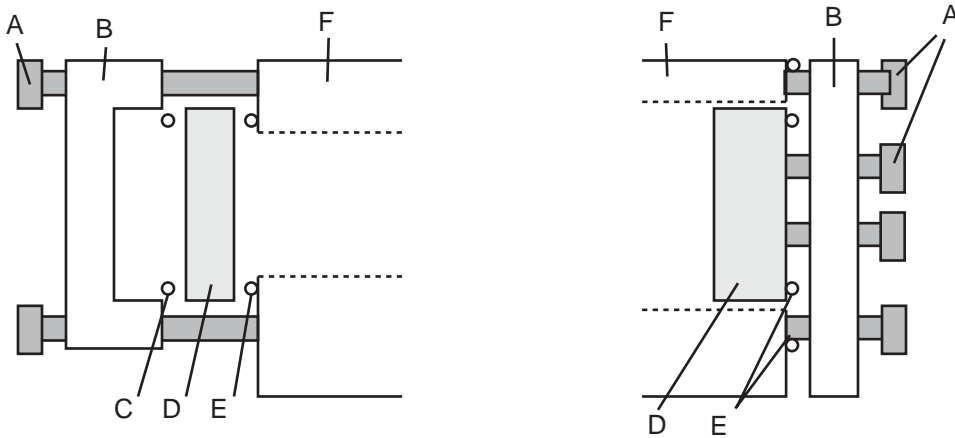
The intensity modulation of the *pump* beam is provided by an SR540 chopper wheel from Stanford Research Systems (www.thinksrs.com). The chopper works with two wheels, for low (400 Hz and below) and high (400 - 4000 Hz) frequencies. The chopper wheel rests on a 2-layer stack of steel and rubber, with resonant frequencies of a few Hz. The stack is enclosed in a box made from 1/8" aluminum sheet metal and lined with closed-cell foam. The best foam is that from the beam scanner's shipping carton. This attenuated the sound by 20 dB at high frequencies. These measures are sufficient to reduce the acoustic coupling of the chopper wheel to the cavity to less than 2×10^{-13} m/rHz at its maximum at 3.9 kHz, which is comparable to the background noise level. Fig. 3.8 compares the rms length-equivalent noise of the interferometer. These data are taken with the *pump* beam blocked.

The manufacturer specifies 0.2° rms phase jitter on the slow wheel and 0.5° rms phase jitter on

the fast wheel, but its long-term phase stability is not so reliable. Therefore, to compute a system's response to the chopper, it's better to add together many short duration samples than to integrate over a long time.

3.2.5.5 Cavity

Figure 3.9: Exploded view of interferometer assembly scheme. Left: input end. Right: "test" end (Aluminum mounting scheme shown). A: bolts, B: clamp, C: O-ring, D: mirrors, E: Indium wire, F: spacer



The interferometer cavity is an Al-6061 spacer block with mirrors attached to the ends (Fig. 3.9). For light to pass through it, the spacer block has a groove cut down the center and holes drilled through the ends. The block is rigidly bolted to a flat aluminum plate, which is clamped to the optical table.

At the front end, the input mirror ($R=95\%$, 50cm radius of curvature) is clamped to the face of the spacer block. The mirror clamp is a block of aluminum with a .75" clearance hole in the center, counter-bored to 1.010"Ø to hold a mirror. A viton O-ring on the back surface and an indium O-ring on the front surface of this mirror hold the mirror snug. At the other end, the mounting scheme varies. For the aluminum mirror (shown), the back of the mirror is bolted to a plate, which is bolted to the cavity. For the other mirrors, an aluminum plate with a hole through the center is affixed to the cavity, and the test mirror is anchored against the plate in the same manner as the input mirror. The mode matching is chosen so that the laser spot radius varies by only 2% for the range of cavity lengths explored in this scheme.

As the spacer block is very sensitive to temperature changes, it has to be shielded from light scattered by the test mirror. The interior surfaces of the cavity are lined with layers of nonconductive

plastic and aluminum foil, so that light scattered by the IFO mirrors will not be absorbed by the sides of the block. The top of the channel is covered with a piece of transparent acrylic to reduce acoustic noise. The laboratory environment is not thermally regulated, so the cavity tends to shrink after sundown – a temperature change of 0.1K is sufficient to sweep the interferometer through one free spectral range! A layer of black foam on the sides and top of the cavity helps minimize conductive heat transparent and slow down its thermal drift. Compensation for thermal drift can also be provided by a heat source, such as an incandescent lamp or a finger on the base of the spacer block.

Near resonance, the IFO input mirror is slightly birefringent, and partially circularizes the beams. Therefore, cross-coupling noise varies somewhat, and is continuously monitored while acquiring data.

3.2.6 Sample preparation

For reasons of expediency and cost, the samples I used varied in their preparations. The BK7, fused silica, and sapphire samples are modifications of standard mirrors and windows purchased from CVI Laser Corp. Aluminum mirrors are sold by several companies, including Polished Metals Ltd. (800-526-7051), Optimum Manufacturing Corp. (800-858-2249), Surface Finishes Co. Inc. (630-543-6682), Opticon (978-663-6105), Optical Filter Corp. (603-357-7662), and Janos Technologies Inc. (802-365-7714).

The gold coatings applied at Caltech were all made at the same time. They were formed by thermal evaporation of gold (.9999) under vacuum. The thickness of the coating was measured to be 180 nm by a crystal rate monitor. A “protected gold” mirror is a proprietary process done by CVI. It starts with a coating of gold, approximately 200nm thick. On top of the gold layer is a thin dielectric layer, to protect the gold from rubbing away. Fig. 3.10 shows a side view of the mirror, and Fig. 3.11 shows a comparison of the length scales.

The thermal conductivity of the Au should not strongly affect the heat flow, as the gold layer conducts much less heat than the substrate or the coating. The radial thermal resistance of a thin disk scales with $1/2\pi\kappa t$, where t is the thickness of the disk. The longitudinal (normal to the mirror surface) thermal resistance scales with t/κ in this direction, the gold coating has much less resistance to heat flow than the layers below it. A summary of thermal impedances is listed in Table 3.2.

All these mirrors scatter a considerable amount of the light that strikes them. The scattered light

Figure 3.10: Side view (not to scale) of sapphire samples. The dielectric stack is the same on the BK7 sample and similar (same number of layers) on the fused silica sample [34]. The gold layers on the other samples have similar opacity, and are likely to have a similar thickness.

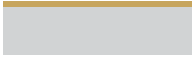
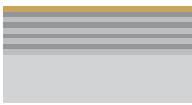
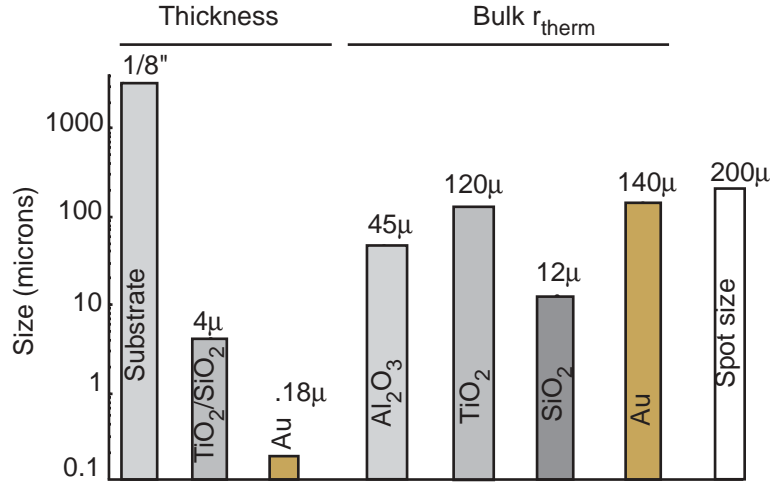
| | Layer | Thickness | r_t (100 Hz) | r_t (1000 Hz) |
|---|------------------------------------|------------------------------|------------------------------|------------------------------|
|  No stack | Au | $1.8 \cdot 10^{-7} \text{m}$ | $4.5 \cdot 10^{-4} \text{m}$ | $1.4 \cdot 10^{-4} \text{m}$ |
| | Al_2O_3 | $3.2 \cdot 10^{-3} \text{m}$ | $1.4 \cdot 10^{-4} \text{m}$ | $.44 \cdot 10^{-4} \text{m}$ |
|  Dielectric stack | Au | $1.8 \cdot 10^{-7} \text{m}$ | $4.5 \cdot 10^{-4} \text{m}$ | $1.4 \cdot 10^{-4} \text{m}$ |
| | $(\text{SiO}_2/\text{TiO}_2)^{15}$ | $4 \cdot 10^{-6} \text{m}$ | $.4 \cdot 10^{-4} \text{m}$ | $.1 \cdot 10^{-4} \text{m}$ |
| | | | $3 \cdot 10^{-4} \text{m}$ | $1 \cdot 10^{-4} \text{m}$ |
| | Al_2O_3 | $3.2 \cdot 10^{-3} \text{m}$ | $1.4 \cdot 10^{-4} \text{m}$ | $.4 \cdot 10^{-4} \text{m}$ |

Figure 3.11: Relative thickness and thermal diffusion length scales at 1000 Hz for the coating layers and substrate. The substrate thickness shown is for sapphire—the other materials had thicker substrates.



intensity is strongest along the direction of the incident beam, so it's rather difficult to measure it. Instead, I estimate the mirrors' reflectivities from their low-frequency response to the photothermal effect.

Table 3.2: The gold layer has less longitudinal thermal resistance than any other layer, and its transverse conductivity is less than that of the TiO₂ layers. For the thin films, t is taken as the lesser of the layer thickness and r_t at 3000 Hz.

| Value | Au film | TiO ₂ film | SiO ₂ film | SiO ₂ substrate | Al ₂ O ₃ substrate |
|---|-----------------------|--------------------------|--------------------------|-------------------------------|---|
| r_t (m) at 3 kHz | 8.2×10^{-5} | 1.5×10^{-5} | 7.1×10^{-6} | 7×10^{-6} | 2.6×10^{-5} |
| κ (W/m-K) | 317 | 300 | 1.4 | 1.4 | 40 |
| t (m) | 1.8×10^{-7} | 1.4×10^{-6} | 2.5×10^{-6} | 7×10^{-6} | 2.6×10^{-5} |
| $1/2\pi\kappa t$ (K/W) (transverse resistance) | 2800 | 370 | 4.5×10^5 | 1.7×10^5 | 28 |
| $2\pi\kappa t$ (W/K) (transverse conductance) | .00036 | .0027 | .00002 | .00006 | .036 |
| t/κ (K m ² /W) (longitudinal resistance) | 5.6×10^{-10} | 4.6×10^{-9} | 3.7×10^{-6} | 5×10^{-6} | 6.5×10^{-7} |

3.2.6.1 Aluminum

The aluminum mirror is a 1" ϕ \times 3/8" block of aluminum, diamond turned on the front surface by Janos Technologies Inc. (www.janostech.com). We do not know exactly what alloy of aluminum was used. The diamond-cutting process leaves the surface reflective, but with visible grooves. Further polishing by CVI Laser Corp. (www.cvilaser.com) attains a uniformly reflective surface of acceptable quality, but with noticeable pits. Care must be taken to protect the reflective surface, which scratches readily from fingers and dust.

The normal-incidence reflectivity of this mirror is 89%. The absorption is around 5%, determined by fitting the DC scale of the photothermal response of the mirror to theory. The balance between absorbed and reflected light is difficult to measure, as the mirror scatters quite a bit of light, most of it along the direction of the incident beam. The back surface is anodized, and presents three #6-32 tapped mounting holes and a central hole used in the manufacturing process. The four holes on the back penetrate about halfway into the mirror.

3.2.6.2 BK7

The BK7 sample with a dielectric stack is a standard flat mirror, part #PR1-1064-99-1037 from CVI. Its substrate is BK7 glass, 1" ϕ \times 3/8" thick. Its front side has a 30-layer, 99% reflective TiO₂/SiO₂

dielectric mirror. Its back side is AR coated. A gold coating was applied to the front surface at Caltech. The normal-incidence reflectivity of this mirror is 95%.

The BK7 sample without a dielectric stack is a protected gold mirror from CVI, part #PG-PM1-1037-C, which has a wedge of a few arcminutes. Its substrate is BK7 glass, 1" \varnothing x 3/8" thick. The normal-incidence reflectivity of this mirror is 96%.

3.2.6.3 Sapphire

The sapphire sample with a dielectric stack is a standard flat mirror, part #PR1-1064-99-PW-1012-SPR from CVI. Its substrate is C-axis sapphire, 1" \varnothing x 1/8" thick. an equivalent substrate, with the same AR coating and dielectric stack as the mirrored BK7 sample. A gold coating was applied to the front surface at Caltech. The normal-incidence reflectivity of this mirror is 97%.

The sapphire sample without a dielectric stack is a C-axis sapphire window, 1" \varnothing x 1/8" thick, part #W1-PW1-1012-SPR-1064-0. It has a an AR coating on its back side, made by CVI. A gold coating was applied to the front surface at Caltech. The normal-incidence reflectivity of this mirror is 97%.

3.2.6.4 Fused silica

The fused silica sample with a dielectric stack is a standard flat mirror, part #PR1-1064-97-PW-1025-UV from CVI. Its substrate is Corning 7980 [34, 35] fused silica, 1" \varnothing x 1/4" thick. Its front side has a 30-layer, $95 \pm 1.5\%$ reflective $\text{TiO}_2/\text{SiO}_2$ dielectric mirror. Its back side is AR coated. It has a protected gold coating on top of its dielectric mirror. The normal-incidence reflectivity of this mirror is 94%.

The fused silica sample without a dielectric stack is a protected gold mirror from CVI, part #PG-PM1-1037-UV, which has a wedge of a few arcminutes. Its substrate is UV grade fused silica, 1" \varnothing x 1/4" thick. It has a protected gold coating on its front surface. The normal-incidence reflectivity of this mirror is 95%.

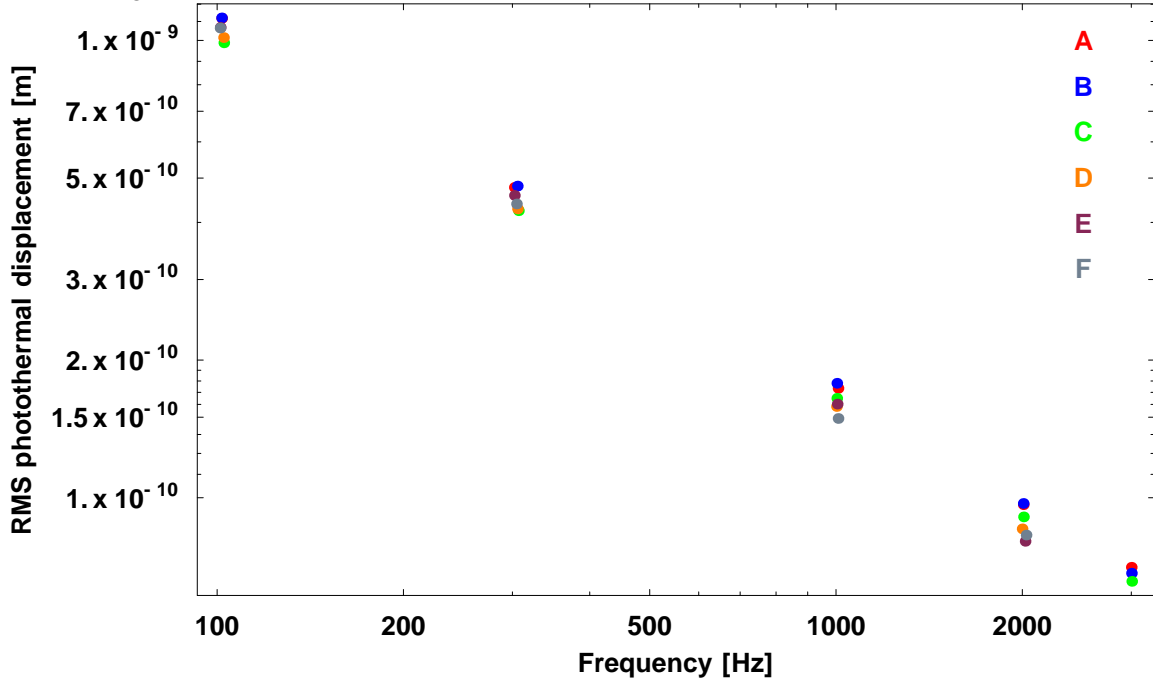
3.2.7 Experimental procedure

3.2.7.1 Configurations

To measure the photothermal effect, the interferometer needs to stay near resonance. The maximum length change Δx that will cause less than a 1% a change in the cavity power is determined by the

condition $\left| \frac{r(1-e^{-i\delta})}{1-r^2e^{-i\delta}} \right|^2 < 0.1$, where $\delta = \frac{2\Delta x}{\lambda}$. For a cavity with a finesse around 100, this is a few nm (Fig. 3.13). This sets the upper limit on the dynamic range for the signal. The practical lower limit on the observable signal is 10^{-11} meters—below this, acoustic noise from the chopper wheel is 2% of the signal magnitude and adds a few degrees of phase to the measurement.

Figure 3.12: Photothermal response of fused silica, for constant *pump* power of 186 mW_{pp}. The servo configurations are listed in table 3.4.



Meanwhile, the magnitude of the photothermal effect varies by a factor 30 between sapphire and metallic aluminum. For each material (Table 3.3), I increased the *pump* power until the rms signal amplitude was greater than 10^{-11} m at the maximum measurement frequency (4 kHz), then I set the servo gain and bandwidth so that the signal amplitude did not exceed the linear range at the minimum frequency (10 Hz). The Al mirror formed a cavity with a finesse of 37, so it had a larger linear range than the other materials.

The *probe* power is limited by the linear range of the RF photodiode (see §3.2.5.2). A neutral density filter in front of the photodiode keeps the power it detects below a mW. This is better than merely reducing the *probe* power, because it's good to have the *probe* beam at the photodiode be more powerful than the cross-coupling fraction of the *pump* beam. A derivation of how cross-coupling noise affects the PDH signal is presented in §5.2 in the appendix.

Figure 3.13: Power transmission coefficient near resonance for a symmetric R=97%, cavity using 1 micron light. To limit power fluctuations to 1%, distance fluctuations need to be less than 4 nm_{pp} .

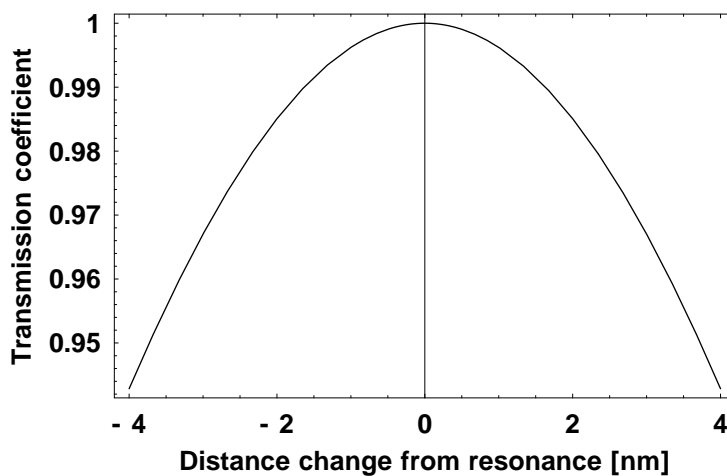


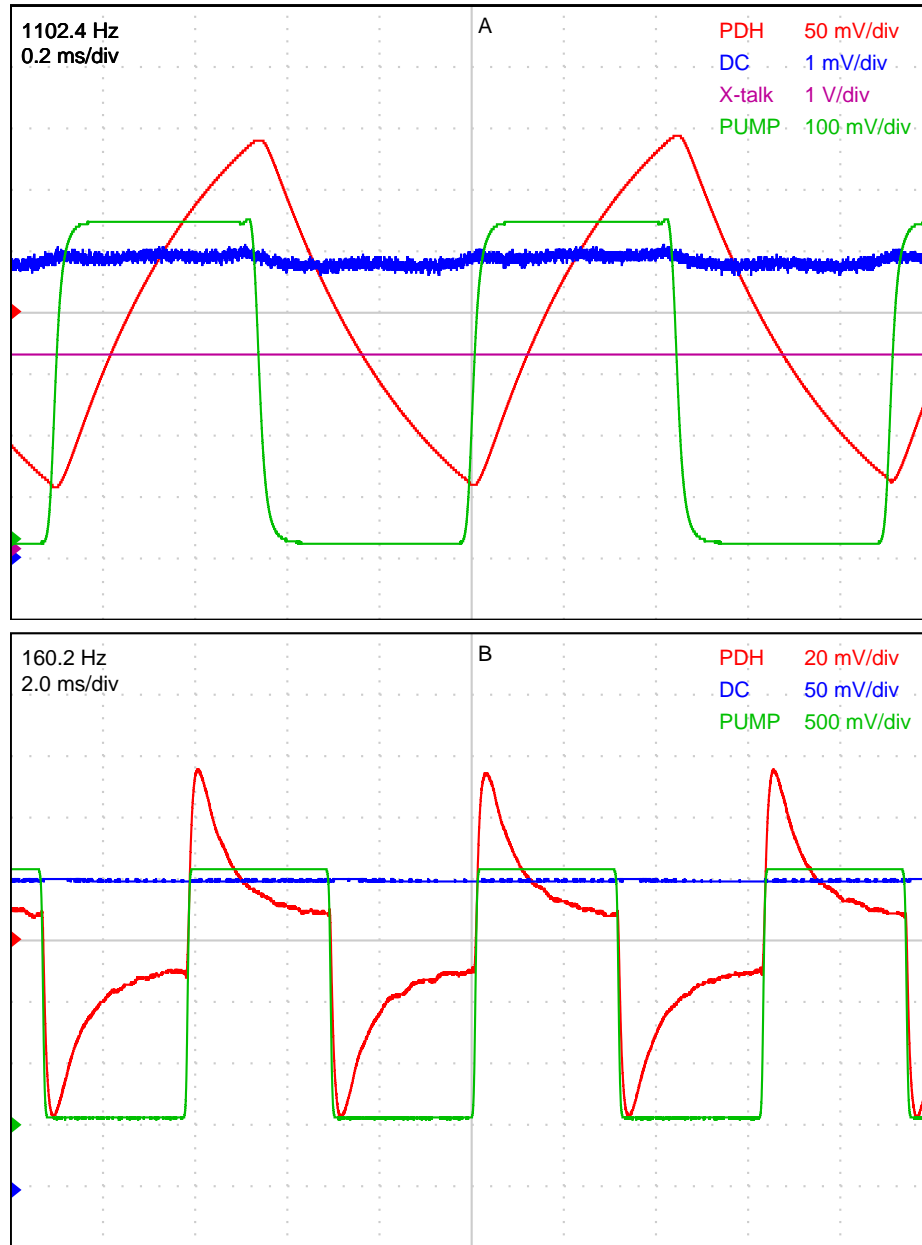
Table 3.3: Optical configurations for each measurement. † Denotes samples with dielectric stacks. Displacements are rms distances measured, above the servo unity gain frequency (UGF). The laser power for the aluminum mirror is unusually high because the cavity visibility was only 50%.

| Material | Pump power | Probe power | Finesse | Servo UGF | min. displacement |
|---------------|------------|-------------|---------|-----------|-------------------------|
| Aluminum | .122 W | .256 W | 37 | 1000 Hz | 3.5×10^{-11} m |
| Sapphire† | .100 W | .058 W | 100 | 140 Hz | 3.5×10^{-11} m |
| Sapphire | .098 W | .058 W | 80 | 240 Hz | 1.9×10^{-11} m |
| BK7† | .020 W | .056 W | 80 | 360 Hz | 1.7×10^{-11} m |
| BK7 | .022 W | .054 W | 67 | 100 Hz | 1.5×10^{-11} m |
| Fused silica† | .176 W | .066W | 70 | 120 Hz | 5.3×10^{-11} m |
| Fused silica | .177 W | .074 W | 70 | 800Hz | 3.9×10^{-11} m |

3.2.7.2 Data acquisition

For each measurement, a Tektronix TDS3014 digital oscilloscope captures (PDH) the PDH signal, (DC) the RFPDs DC output, (X-talk) the lock-in amplifier's magnitude reading, and (PUMP) the voltage from the photodiode monitoring the chopper. The scope takes 10,000 data points per sample with 8 bits precision, averaging up to 512 samples together by triggering on the rising edge of the chopper monitor photodiode (Fig 3.14). The lock-in amplifier measures the DC port of the RFPD ($\times 50$ for the Aluminum measurement) at the frequency of the chopper's TTL output, and produces from its front panel a voltage proportional to the rms magnitude of the voltage fluctuations. At the end of a data capture, all four waveforms are copied through the serial port to a notebook computer

Figure 3.14: (A) Thermal expansion and cooling of gold-coated sapphire, with a full range of 2.5×10^{-10} m. Red: The filtered PDH signal (8.7×10^{-10} m/V). Blue: RFPD DC voltage shows a small cross-coupling. Purple: rms amplitude of the blue channel, measured with a lock-in amp. Green: chopper-monitor photodiode. (B) Data for the aluminum sample below the servo's unity gain frequency. Thermal diffusion acts quickly to expand or compress the cavity, and the servo acts slowly in the other direction.



separately with the network analyzer (see §3.2.4 for details on correcting for the servo).

3.2.7.3 Computation

Figure 3.15: Intermediate data for gold-coated sapphire. A: PDH voltage magnitude. B: Blue: PDH phase relative to scope trigger point. Red: chopper phase relative to scope trigger point. Black: blue - red.

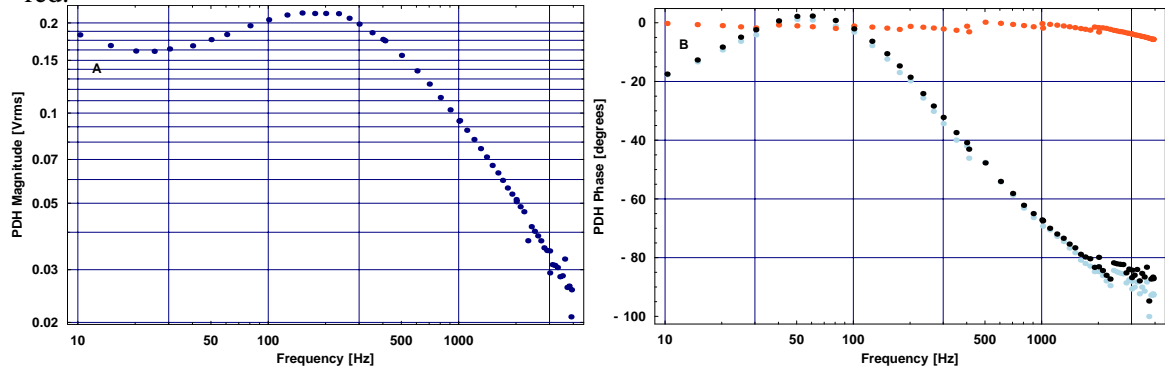
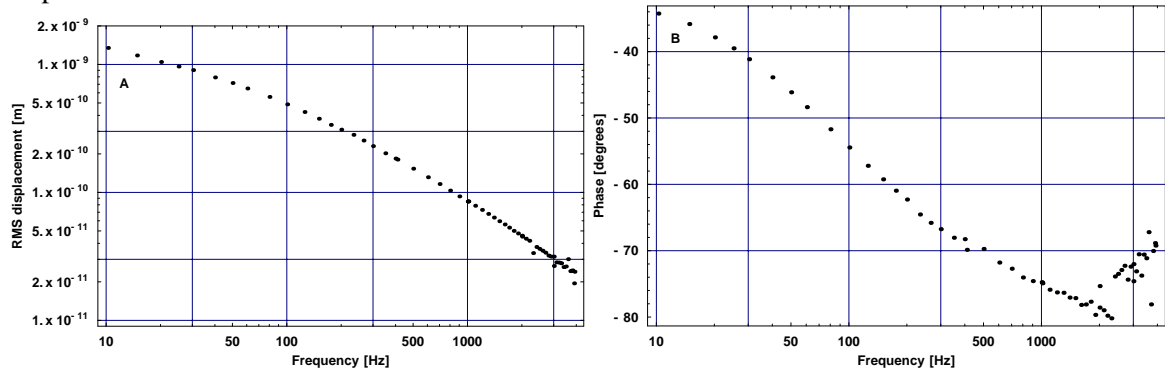


Figure 3.16: Intermediate data for gold-coated sapphire. A: Sample displacement. B: Sample phase response.



Since heat diffusion is a linear system, we can easily analyze it in the frequency domain. At several frequencies between 10 and 4000 Hz, I compute the primary Fourier component of the cavity's frequency response and compare it to the primary component of the *probe* beam's oscillating power.

Taking a time series d_n from a data file, the rms sin and cos components of the waveform at the chopper frequency f are obtained by averaging over an integral number of chopper cycles.

$$s(f) = \sqrt{2} \sum_{n=1}^m (d_n - \langle d \rangle) \sin\left(2\pi \frac{n \times \text{cycles}}{m}\right)$$

$$c(f) = \sqrt{2} \sum_{n=1}^m (d_n - \langle d \rangle) \cos(2\pi \frac{n \times \text{cycles}}{m})$$

The rms amplitude of the displacement is simply $\sqrt{s^2(f) + c^2(f)}$, and its phase relative to the oscilloscope trigger point is $\arctan(c(f)/s(f))$. The rms amplitude of the driving thermal force is $P_0 \frac{\sqrt{2}}{\pi}$, where P_0 is the peak-to-peak amplitude of the square-wave *pump* beam fluctuations.

All the measurements for a sample run are stored in a single data file. The first step in analyzing the data is to calculate the magnitude of the PDH signal (PDH) and its phase relative to the chopper wheel (PUMP) (Fig. 3.15). The chopper frequency f is measured by the scope and saved with the waveform. Next, the data are scaled by the calibration factor, and both magnitude and phase are compensated for the effects of the servo (see §3.2.4) (Fig. 3.16).

3.2.7.4 Scattering

All the test mirrors scatter light, much of which appears to travel in a cone near the reflected beam. An apparatus to measure this is shown in Fig. 3.17. The test mirror is mounted on a rotary stage, and a laser beam is aimed at the mirror. A photodiode, as near to the incident beam as possible and .32 m from the mirror, measures the reflected light power at near-normal incidence. The photodiode response is determined by comparing it to a known 350 mW beam attenuated approximately 100,000 times by neutral density filters. The detector (ThorLabs DET110, [115]) has an area of 13 mm², which subtends a solid angle of $\sim 5.8 \times 10^{-4}$ steradians, or a linear angle of .7°.

Measured data are shown in Fig. 3.18 for the gold-coated plain sapphire substrate, with the power measured by the photodiode plotted against the rotation angle of the test mirror (see Fig. 3.17). The reflection off the mirror shows an asymmetric distribution of scattered light. To estimate the total scattered power, I convert the measured power at an angle θ to a power density on an annulus of diameter $\sin \theta$. Using a linear interpolation between these points, the integrated power is calculated to be ~ 2 mW.

3.2.7.5 Power absorption

Comparing the data to models requires an estimate of the power absorbed by the test mirror, P_{abs} . This, in turn, depends on the *pump* light power, the coupling of the *pump* beam to the cavity, and the absorptivity of the sample. Of these three quantities, the latter must be inferred from the data.

Conservation of energy requires that the light power incident on the cavity be either reflected,

Figure 3.17: Measuring scattering from a test mirror. The beam, at angle 0, is $\sim 1^\circ$ wide.

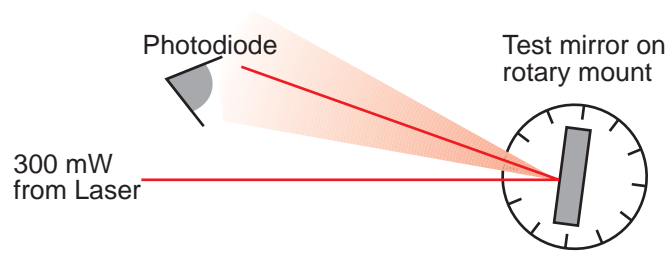
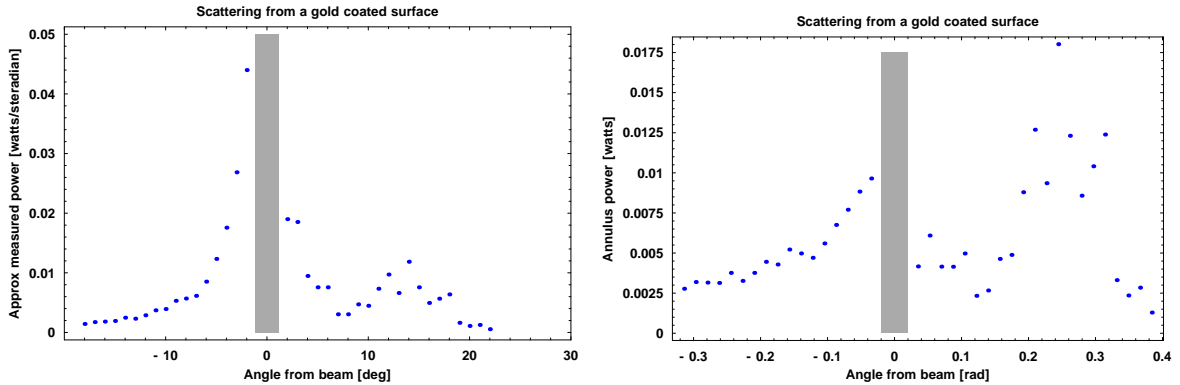


Figure 3.18: Measuring scattering from a gold-coated sapphire mirror. The gray bars show the angles near the reflected beam. Left: scattered power per steradian as a function of angle from the reflected beam center. Right: scattered power per radian for a circular annulus, as a function of angle from the reflected beam center.



scattered, or absorbed.

$$P_{reflected} + P_{abs} + P_{scattered} = P_{pump} \quad (3.3)$$

Two of these terms are known: P_{pump} is measured with a power meter, and the ratio $P_{reflected}/P_{pump}$ is found by sweeping the laser frequency slowly through resonance and measuring the power in the reflected beam. Note that $P_{reflected}$ is the reflection from the cavity, not from the sample mirror. This determines the cavity's visibility, the fraction of power that is not reflected. Neglecting losses at the cavity input mirror and from absorption by air, this can only be accounted for by absorption or scattering off the sample mirror.

$$visibility = \frac{P_{abs} + P_{scattered}}{P_{pump}} = 1 - \frac{P_{reflected}}{P_{pump}} \quad (3.4)$$

The reflectivity of the sample mirror is measured outside of the interferometer. Knowing the sample reflectivity R , where $R < 1$, the sum of the sample's absorption and scattering coefficients, A and S , is determined by $A + S = 1 - R$. Assuming the cavity's scattering and absorption occurs only at the sample mirror, we can define P_0 as the power incident on the sample.

$$P_{abs} = P_0 A \quad (3.5)$$

$$P_{scattered} = P_0 S \quad (3.6)$$

Combining this with Eq. 3.4, we get the equation

$$visibility \times P_{pump} = P_0 A + P_0 S \quad (3.7)$$

By solving for P_{abs} , we can express the power absorbed by the mirror in terms of the unknown absorptivity coefficient A and other, known quantities.

$$P_{abs} = visibility \times P_{pump} \times \frac{A}{1 - R} \quad (3.8)$$

In plotting a model against the data, A is free parameter constrained to be less than $1 - R$.

3.2.7.6 Systematic errors

As you can see in Fig. 3.14, the precise locations of the chopper transitions are somewhat ambiguous. The beam radius at the chopper is .13 mm at the chopper, and the gaps in the fast wheel are only 8 mm wide. I calculate the systematic phase error as one-half the difference between the positive and negative duty cycles of the PUMP signal. The algorithm to determine this measures the elapsed times for one full cycle between the positive-going and negative-going edges at the mean value of the waveform. This is about 4° for the fast chopper wheel and 1° for the slower one. Error bars based on the measured phase error are plotted in the Results section.

The major known systematic error in the magnitude is cross-coupling noise, which depends on the amount of *pump* light reflected from the cavity that reaches the RFPD. The RF and DC components of the PDH signal both depend on a random phase ϕ and the crosstalk factor, ζ , where

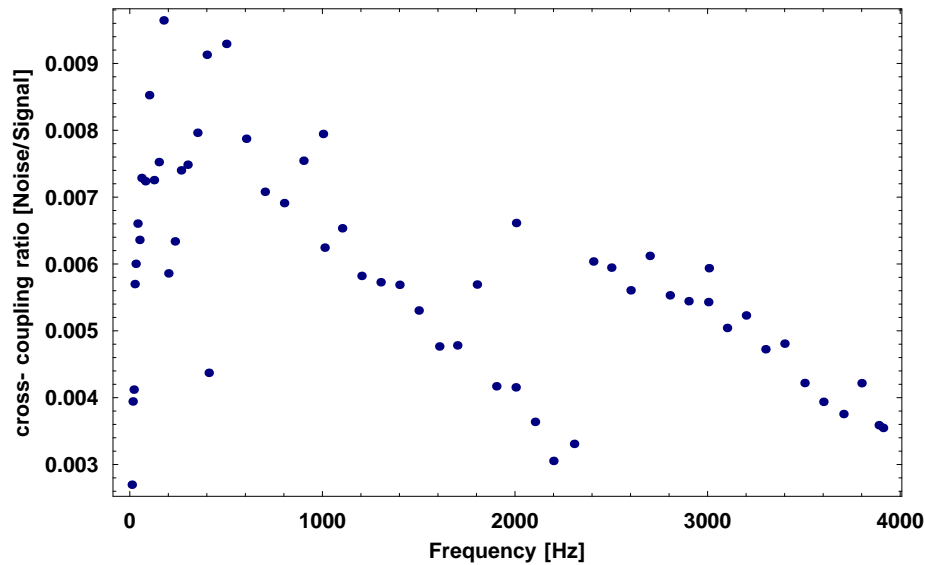
ζ^2 is the fraction of *pump* light which reaches the RFPD. The unknown phase shift ϕ reflects the path difference between the *pump* and *probe* paths, and varies with thermal expansion of the optics table and the optics mounting hardware.

$$P_{RF} \propto 2\sqrt{P_S}(\sqrt{P_C} + \zeta\sqrt{P_F} \cos \phi) \quad (3.9)$$

$$P_{DC} \propto (\zeta^2 P_F + P_C + 2\zeta\sqrt{P_F P_C} \cos \phi) \quad (3.10)$$

where P_S and P_C are the *probe* beam sideband and carrier powers, and P_F is the *pump* beam power (see §5.2). Since $P_C \gg P_F$ at the RF photodiode and $\zeta \ll 1$, the ζ^2 can be neglected, and the fractional measurement error in the PDH signal is proportional to $\zeta \cos \phi \sqrt{P_F/P_C}$, and fractional variation in the voltage measured by the RFPD is $2\zeta \cos \phi \sqrt{P_F/P_C}$. We can monitor the latter by hooking up the RFPD's DC output ($\langle V \rangle$) to a lock-in amplifier, triggered off the chopper. The lock-in amplifier measures the rms amplitude of the fundamental mode of the variations (V_{rms}), which are recorded by the oscilloscope. The cross-coupling factor (noise/signal ratio) is computed as $V_{rms}/\langle V \rangle$. This factor was measured for every data point, and is usually less than 1% (Fig. 3.19). The interferometer input mirror is slightly birefringent, so ζ varies if the cavity strays far from the center of its resonance. To combat this, operator intervention is effective at regulating the laser and cavity temperatures on sub-Hz timescales.

Figure 3.19: Cross-coupling noise ratio for gold-coated sapphire.



The calibration process depends on fitting the measured OLTF to a model of the servo, and this process can introduce error due to noise in the measured transfer functions. To estimate this uncertainty, I repeated a measurement several times with different servos, *probe* powers, sideband modulation depths, and attenuation factors at the RFPD. Labelled A-F, they are listed in table 3.4 and the data are plotted in Fig. 3.12. Runs A-D used the *probe* beam at full power (70 mW), with sideband modulation depth at its typical level (3% power in each sideband) and a 1/100 attenuator at the RFPD. Runs E-F used the *probe* beam at half power (36 mW), with sideband modulation depth at 1/10 of its typical level and only a 1/10 attenuator at the RFPD. The D, E, and F runs are missing points at 3 kHz because of errors in transferring data from the oscilloscope to the computer.

The spread in these data suggests that the imprecision of the calibration process is about 10-15%, likely due to errors in measuring the servo transfer function, which sets the overall calibration of the instrument.

Table 3.4: Six servo configurations for measuring the response of dielectric-coated fused silica, for constant *pump* power of 186 mW_{pp}.

| Label | <i>Probe</i> power mW | Servo UGF kHz | Servo DC Gain | 100Hz displacement 10^{-9}m_{rms} | 2kHz displacement 10^{-11}m_{rms} |
|-------|--------------------------|------------------|------------------|---|---|
| A | 70 | 1 | 30 | 1.12 | 9.65 |
| B | 70 | 2.6 | 75 | 1.12 | 9.72 |
| C | 70 | 23.8 | 83 | .99 | 9.08 |
| D | 70 | 5.6 | 15 | 1.01 | 8.55 |
| E | 36 | 1.8 | 61 | 1.07 | 8.03 |
| F | 36 | .44 | 16 | 1.06 | 8.29 |

3.3 Results

The data analysis process produces a set of complex numbers corresponding to the magnitude and phase of each sample's displacement, which can be compared to the theoretical model described by Cerdonio *et al.* [32]. The frequency response this predicts for the average displacement $D(f)$ of the mirror surface is given by the equations

$$D(f) = \frac{\sqrt{2}\alpha(1+\sigma)P_{abs}}{\pi\kappa} \times \frac{1}{\pi} \int_0^\infty du \int_{-\infty}^\infty dv \left[\frac{u^2 e^{-u^2/2}}{(u^2+v^2)(u^2+v^2+if/f_c)} \right] \quad (3.11)$$

$$f_c = \frac{\kappa}{2\pi r_0^2 \rho C_p}$$

The first part of Eq. 3.11 determines the scale of the mirror displacements and depends on P_{abs} , the rms power absorbed by the mirror. The second part, under the integral signs, determines the frequency dependence of $D(f)$. In the limit of high frequencies, this approaches the Braginsky, Gorodetsky, and Vyatchanin (BGV) equation [22].

$$D_2(f) = \frac{\sqrt{2}\alpha(1+\sigma)}{\pi} \frac{P_{abs}(f)}{(\rho C_V \pi r_0^2) i f} \quad (3.12)$$

This equation has a constant phase of -90° , while the phase of Eq. 3.11 varies from zero at DC to -90° at high frequencies.

After applying the calibration and compensating for the servo, as described in §3.2.7.3, the data describe the root-mean-square (rms) amplitude of the fundamental component of the measured displacement. Meanwhile, the *pump* beam power is measured as the peak-to-peak (pp) range of a square wave. The rms amplitude of the fundamental mode of a square-wave signal can be deduced from the Fourier decomposition of a square wave H_{sq} with a peak-to-peak range of B .

$$H_{sq} = \sum_{\text{odd } n=1}^{\infty} \frac{2B}{n\pi} \sin n\omega t \quad (3.13)$$

The rms amplitude of a sine wave is $1/\sqrt{2}$ of its peak amplitude, so we obtain the following conversion formula:

$$V_{rms}^{sine} = V_{pp}^{square} \frac{\sqrt{2}}{\pi} \quad (3.14)$$

The various sample materials were tested under different conditions, with different laser powers, interferometer visibility, and coating reflectances. Fortunately, the circumstances were similar between samples with the same substrate. Table 3.5 summarizes these configurations, and the following sections discuss the results for each of the materials examined.

Table 3.5: Conditions for photothermal measurements. † Denotes samples with dielectric stacks. The A values are the absorptivities obtained from fitting the predicted substrate response to the data.

| Sample | Coating type | Pump power (mW _{pp}) | visibility (%) | R (%) | A (%) |
|---------------|--------------|--------------------------------|----------------|---------|---------|
| Aluminum | plain | 122 | 49 | 89 | 6.5 |
| Sapphire† | Au | 100 | 72 | 97 | 1.5 |
| Sapphire | Au | 98 | 72 | 97 | 1.5 |
| BK7† | Au | 20 | 86 | 97 | |
| BK7 | protected Au | 22 | 87 | 96 | 2.6 |
| Fused silica† | protected Au | 176 | 82 | 94 | |
| Fused silica | protected Au | 177 | 91 | 95 | |

3.3.1 Aluminum

The aluminum mirror was chosen to debug the instrument because of its large thermal expansion coefficient. We expected to find its photothermal response closely following Eq. 3.11, but the frequency dependence of the data was different than predicted for Al 6061-T6⁹. The data are plotted in Fig. 3.20, along with the model, where the absorptivity was fit to the data. The dashed line in the magnitude plot is Eq. 3.11 uses the parameters for Al 6061-T6 listed in table 2.3.

This alloy of aluminum is known to change its properties with working [3], so the polishing and anodizing it received during its manufacture may have affected its thermal properties. If thermal conductivity is allowed to vary as a fit parameter, we get the solid black line in Fig. 3.20, which agrees well with both the measured magnitude and phase.

To make this fit, I replaced the factor κ/r_0^2 in f_c with $a\kappa/r_0^2$ computed Eq. 3.11 for a range of

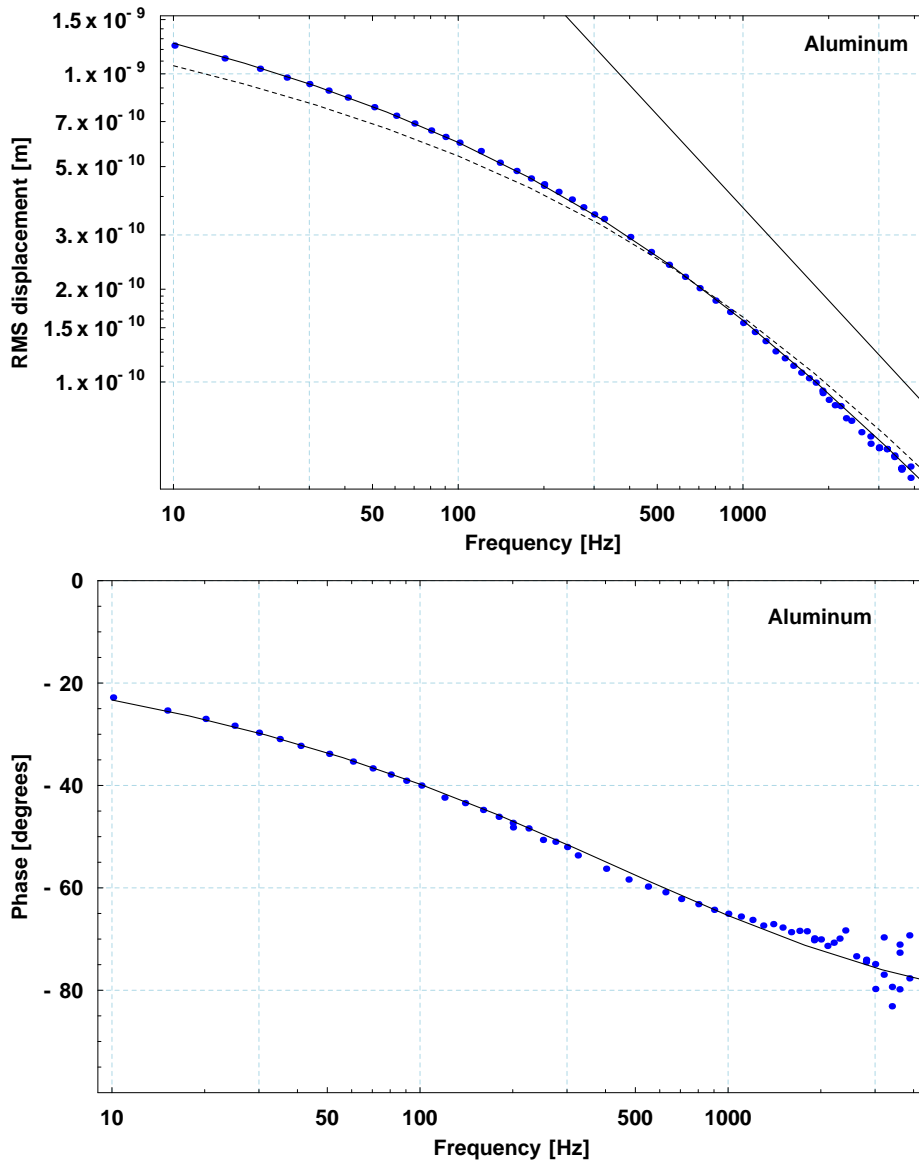
⁹Alloy number 6061, temper number 6

values of a at the each of the frequencies at which I had data points. Interpolating between these calculated values for the model gives a best fit value of a of 0.67. If this were due entirely to a change in thermal conductivity, that would be surprisingly low, but not impossible for an aluminum alloy¹⁰. This factor could also be caused by a higher heat capacity than usual or a larger laser spot than expected.

The straight solid line in the magnitude plot of Fig. 3.20 shows the BGV equation (Eq. 3.12), which has a $1/f$ dependence.

¹⁰Alloy 5456 has a thermal conductivity around 120 W/m-K [113]. The Aluminum Association has this to say about its published tables of materials data: “The following typical properties are not guaranteed since in most cases they are averages for various sizes, product forms, and methods of manufacture and may not be exactly representative of any particular product or size. These data are intended only as a basis for comparing alloys and tempers and should not be specified as engineering requirements or used for design purposes” [113]

Figure 3.20: Photothermal displacement magnitude and phase for aluminum. The solid line fit to the data in the magnitude and phase plots shows the photothermal effect, with the ratio κ/r_0^2 fit to the data in addition to the mirror absorption. The dashed line shows the predicted response based on material parameters in table 2.3, fit only to the mirror absorption. The straight line is the BGV formula, which sets the upper frequency limit



3.3.2 Sapphire

Sapphire is a much more standard material than aluminum, and is thus better for demonstrating this instrument. There are two sapphire samples, one with and one without a 99% reflective dielectric stack, both covered with 97% reflective layers of pure gold, 180 nm thick. We expect the sample without a stack to follow the Cerdonio *et al.* formula, Eq. 3.12 without adjusting any of the material parameters.

The sample with the stack should have a response like that of the substrate, plus an additional contribution from the coating. The coating response function derived in §2.4.2.1 is repeated here.

$$D_c(f) = \frac{\alpha_{layer} \tilde{P}(\omega)}{\rho C_v \pi r_0^2 i \omega} \left(1 - e^{-d \sqrt{i \omega / a^2}}\right)^2 \quad (3.15)$$

Fig. 3.21 shows the measured displacement magnitude and phase for sapphire, with (blue) and without (orange) dielectric stacks. The solid line through the orange points is the model of the substrate, fit only to the mirror absorption, and using the material properties listed in table 2.3. The solid line through the blue points is the model of the substrate using the same parameters as the other line, plus the coating. The best fit for the mirror absorption is 1.5% for both curves, and the coating thermal expansion fit gives $\alpha_{layer} = 24 \times 10^{-6}/\text{K}$.

The “upper limit” lines show the BGV model of the photothermal effect, using the substrate and coating material properties. The former is the asymptotic limit for the substrate, the latter is the asymptotic limit for the coating itself. The “dielectric stack” line shows the magnitude of $D_c(f)$, the model for the coating response. We expect the response of the dielectric stack to converge to the “coating upper limit” line somewhere above 10 kHz, where the thermal diffusion length in the coating becomes much less than its thickness.

Both samples agree well with the Cerdonio *et al.* theory (Eq. 3.11) below 100 Hz, while the sample with a dielectric stack shows a discernable additional expansion above 500 Hz. At 1 kHz, the coating thickness is about 30% of its thermal diffusion length, and it increases the photothermal expansion by around 10% over the substrate expansion. The model for the expansion of the substrate with a coating is not in perfect agreement with data, but it comes very close to the measured magnitude response and within a few degrees of the phase. The phase response of the substrate deviates from the model when the signal strength is around 3×10^{-11} m, which may be due to

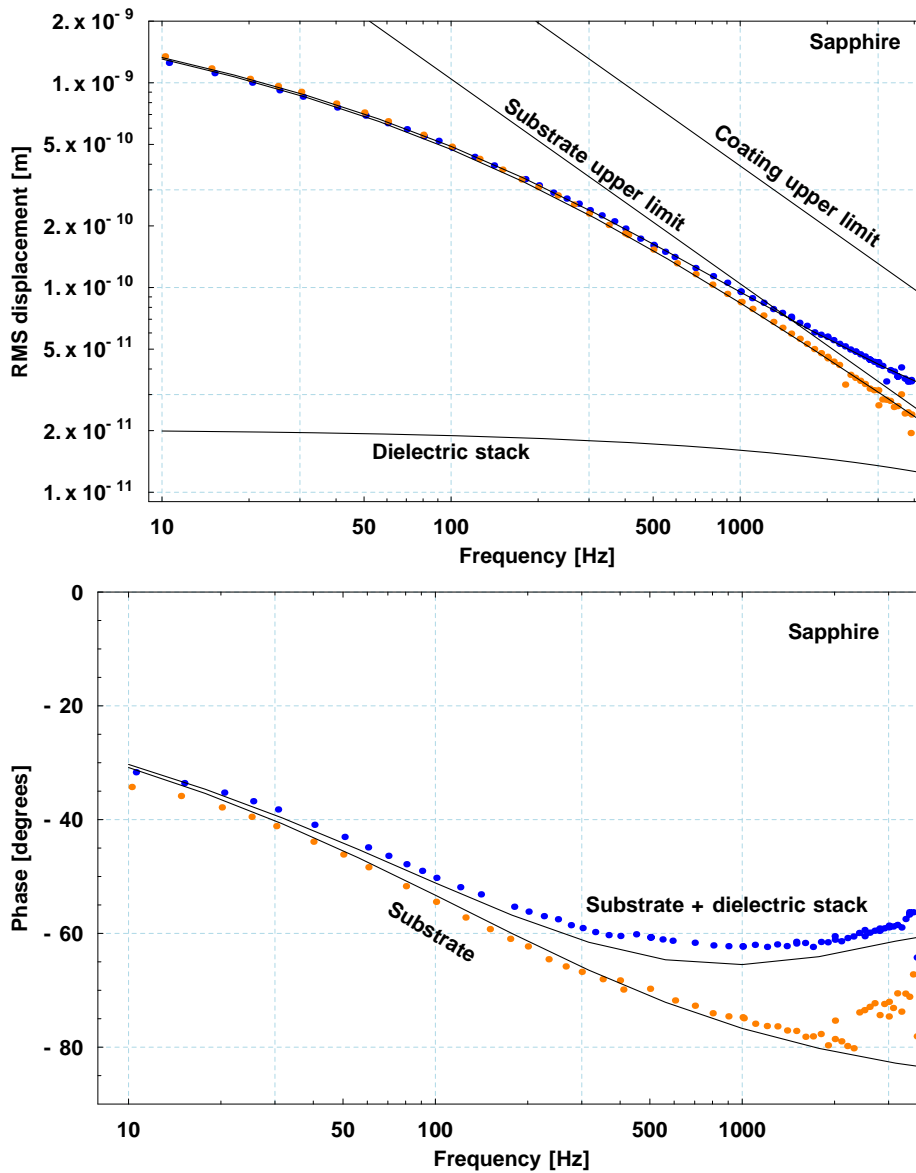
acoustic noise or mechanical resonances in the interferometer spacer hardware.

In calculating the model for the coating, the coating is assumed to be a homogenous layer, with its thermal properties averaged from its constituents, SiO₂ and TiO₂. The coating's effective thermal conductivity is 2 W/m-K, obtained from Eq. 2.3, where d_1 and d_2 are the lumped thicknesses of the coating layers. The average density is taken to be 3000 kg/m³, and heat capacity to be 700 J/kg-K. Thin TiO₂ thin films, which make up 40% of the coating thickness, have been reported to have a thermal expansion coefficient of $50 \times 10^{-6}/\text{K}$ [56], and the SiO₂ layers are believed to have a thermal expansion coefficient around $1 \times 10^{-6}/\text{K}$ [127]. Combining these as a weighted average, the expected value of α_{layer} is $20 \times 10^{-6}/\text{K}$. The expansion is clearly dominated by the TiO₂ layers, whose expansion is much greater than that of SiO₂¹¹. These expected parameters should of course be treated with a grain of salt, since we can't peel off the coatings, dissect them, and measure their layers independently.

The observed data do not rule out the possibility that stress effects enhance the thermal expansion. Notably, the data are not consistent with Eq. 2.43, or any similar theory with a displacement response proportional to $1/\sqrt{f}$.

¹¹The generally accepted value for the thermal expansion of SiO₂ is $0.5 \times 10^{-6}/\text{K}$, but higher values have been found in non-thermally grown films [5, 20, 30, 127]

Figure 3.21: Photothermal displacement magnitude and phase for sapphire, with (blue) and without (orange) dielectric stacks. The orange points are compared to a model of the substrate, fit only to the mirror absorption. The blue points are plotted against the same substrate model plus a fit to the coating (plotted separately as the “dielectric stack” line). The mirror absorption is taken to be 1.5% for both curves, and the coating thermal expansion fit gives $\alpha_{layer} = 24 \times 10^{-6}/\text{K}$. The “upper limit” lines are the BGV model, using the substrate and coating material properties.



3.3.3 BK7

The BK7 samples have the greatest photothermal response, and the sample with the 99% reflective dielectric stack expands more than the substrate. The sample with the dielectric stack was given a gold coating at Caltech at the same time as the sapphire samples, and the sample without the dielectric stack is a commercially available protected gold mirror.

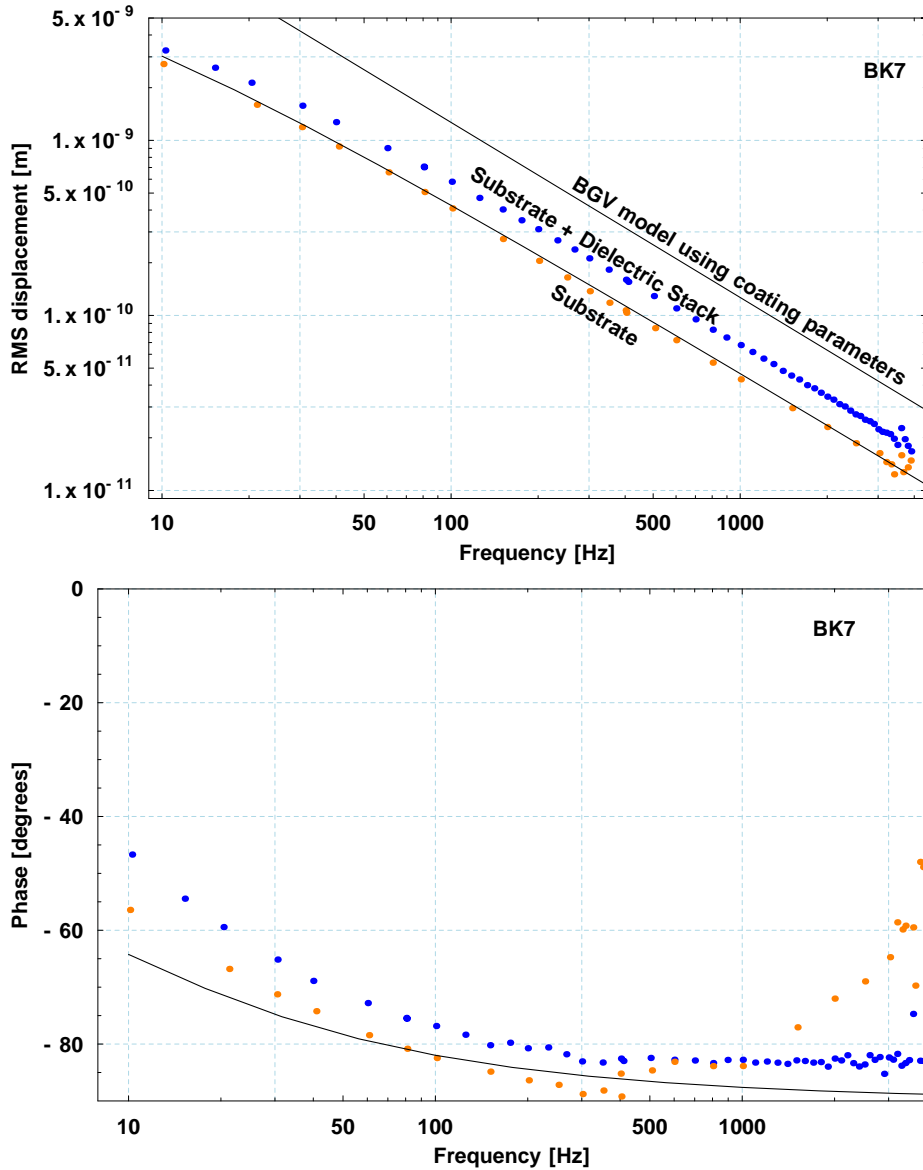
Fig. 3.22 shows the measured displacement magnitude and phase for BK7, with (blue) and without (orange) dielectric stacks. The solid line through the orange points is the model of the substrate, fit only to the mirror absorption, and using the material properties listed in table 2.3. The phase of this model is plotted against the phase data. The best fit for the mirror absorptivity is 2.6% for the sample without the dielectric stack.

The sample with the dielectric stack (blue) shows considerably more expansion than does the substrate. The upper line in the magnitude plot shows the BGV limit of the photothermal effect, using the same average coating parameters as for the sapphire plots¹². The response of this sample is inconsistent with Eq. 2.45 derived in Chapter 2, which predicted a $1/\sqrt{f}$ spectrum for the coating's contribution to thermal expansion. This theory is based on calculating the temperature profile in a homogenous media, and then computing the average fluctuation in a zone near the surface. If we evaluate the model derived for the sapphire substrate, Eq. 3.15, we get a magnitude for the coating expansion of less than 10^{-11} m, so the assumptions used to derive that model clearly do not apply to this situation.

Instead, these data could be interpreted as observations of part of a gradual transition from a low frequency range (~ 10 Hz) where the substrate dominates to a high-frequency range (> 10 kHz) where the coating response dominates.

¹²The laser power was different between the BK7 and sapphire measurements

Figure 3.22: Photothermal displacement magnitude and phase for BK7, with (blue) and without (orange) dielectric stacks. The upper solid line in the magnitude plot is the BGV model, using the coating's average thermal properties. The lower solid line is a model of the substrate's photothermal response.



3.3.4 Fused silica

Both fused silica samples have Corning 7980 [35] substrates, and were manufactured by CVI Laser. One sample has a 95% reflective dielectric stack on top of the substrate, and both are covered with commercial protected gold coatings.

Fig. 3.23 shows the measured displacement magnitude and phase for fused silica, with (blue) and without (orange) dielectric stacks. The solid line below the orange points in the magnitude and phase plots is the model of the substrate, assuming the mirror absorptivity to be 4% and using the material properties listed in table 2.3. The upper line in the magnitude plot shows the BGV limit of the photothermal effect, using the same average coating parameters as for the sapphire plots.

The data for the fused silica samples present a surprise, since their measured magnitude response is a few times greater than expected. Repeated measurements of the fused silica samples with varying *pump* and *probe* beam powers show that the signal is linear with respect to the *pump* power, and it does not scale with the *probe* power. This suggests that the extra thermal expansion is a linear effect, correlated with the power absorbed by the fused silica mirror.

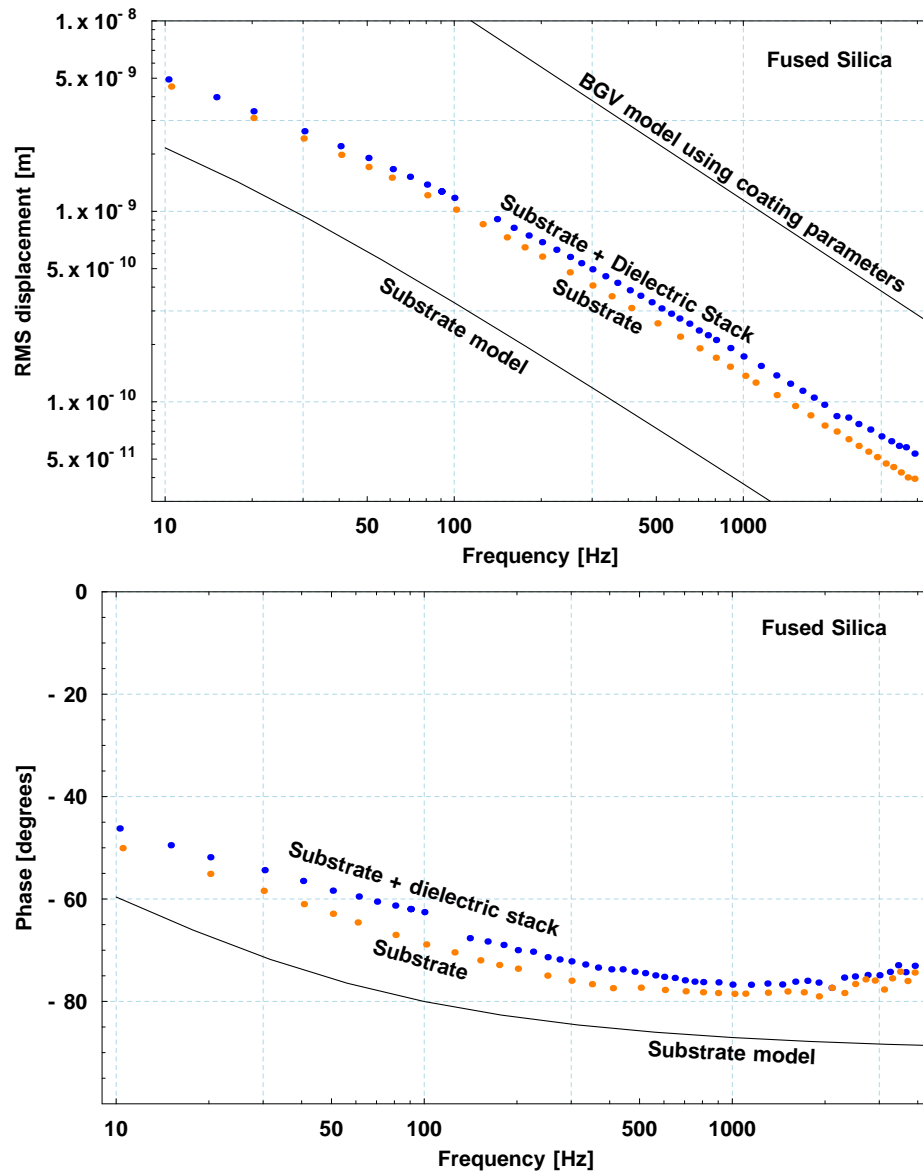
A possible cause for the unusually high readings in fused silica could be the “protected gold” layer, since light in the interferometer has to pass twice through a clear protective coating on top of the gold. If the protective coating had a large, negative dn/dT coefficient, this could account for some of the excess expansion of the samples. The optical path length change due to the protective layer is $\Delta L = 2 \times nd(\alpha + \beta)\Delta T$, where $\beta = dn/dT$. If the temperature change is 10 K, β is -10^{-5} and the layer’s optical thickness is $nd \sim 10^{-6}$ m, heating of the layer could affect the cavity’s measured length by around 2×10^{-10} m. Unfortunately, the protective coating is a trade secret [34] and measurements of its properties are not available to us, but -10^{-5} is not an unreasonable value for β for some materials [49]. A useful experiment would be to repeat these measurements on samples coated with bare gold.

It is unlikely that scattered light expanding and contracting the interferometer hardware would account for the excess signal. Expansion of the spacer block has the wrong sign, expanding the cavity when the mirror’s expansion would shorten it. The phase of the fused silica data would be different by 180° if this effect exceeded the substrate’s thermal expansion. Also, the procedures and software algorithms used to compute and analyze the fused silica data are identical to those used on the sapphire and BK7 samples.

As with the BK7 samples, the sample with the dielectric coating expands more than the one

without, and this difference increases with frequency.

Figure 3.23: Length and phase response of fused silica mirrors, with (blue) and without (orange) dielectric stacks. The model lines is based on absorbed power of 4%.



3.3.5 Summary

The purpose of this experiment is to test our understanding of the photothermal effect in dielectric-coated mirrors. A secondary goal is to set bounds on the thermal expansion coefficient of a mirror coating. While methods exist for measuring the thermal expansion of thin films [66, 118], there is very little work on entire dielectric stacks. The dielectric coating measurements by Braginsky and Samoilenko use the bending beam method [25], and depend on accurate values of the coating's Young's modulus. The method developed in this thesis allows a direct measurement of a mirror's thermal expansion as it would be detected by a Gaussian laser beam. By varying the *pump* beam power, this technique is able to measure behaviors that span more than 2 orders of magnitude in surface displacement and 3 orders of magnitude in frequency.

Being able to vary the *pump* power by an order of magnitude also helps inspire confidence that these experiments measure linear effects. The photothermal transfer functions for these materials, which has units of displacement per unit power absorbed, are plotted in Fig. 3.24. These curves are obtained by dividing the measured data described above by the rms power absorbed by the sample without a dielectric stack, as determined by fitting the model for the substrate expansion to the data. In the case of the fused silica data, a mirror absorptivity of 4% is assumed for this normalization.

Of these materials, the photothermal effect is the smallest for fused silica, even with its unexpectedly high measured response. To demonstrate the linearity of fused silica in these experiments, Fig. 3.24 shows two overlapping curves for the fused silica sample without a dielectric stack, taken during different months and with different *pump* beam powers.

In all of these materials, a dielectric stack makes a significant contribution to the photothermal response of a mirror. To visualize the coating's effect, Fig. 3.25 compares the ratio of photothermal displacement of samples with dielectric stacks to those without. This plot is obtained by generating two functions, $g_c(f)$ and $g_s(f)$, which are linear interpolations of the magnitude data for the samples with and without dielectric coatings, respectively. The ratio $r = \gamma g_c(f)/g_s(f)$ is plotted, with γ chosen to normalize r to 1 at 25 Hz.

The effect of the coating is most notable in sapphire, even though all three data sets compare samples with similar dielectric stacks. From this, I conclude that the choice of substrate material affects the coating photoelastic effect, and that further theoretical work is indicated to understand how.

Figure 3.24: Normalized response (displacement divided by *pump* beam power) of BK7, sapphire, and fused silica for a .2mm spot radius (1/e power). The fused silica data are higher than expected. The dark lines on top are the samples with dielectric stacks; the lighter lines on the bottom are the samples without dielectric stacks. Of the lower fused silica substrate data, the light dashed line was taken with *pump* power 19 mW, and the sold line with *pump* power 174 mW.

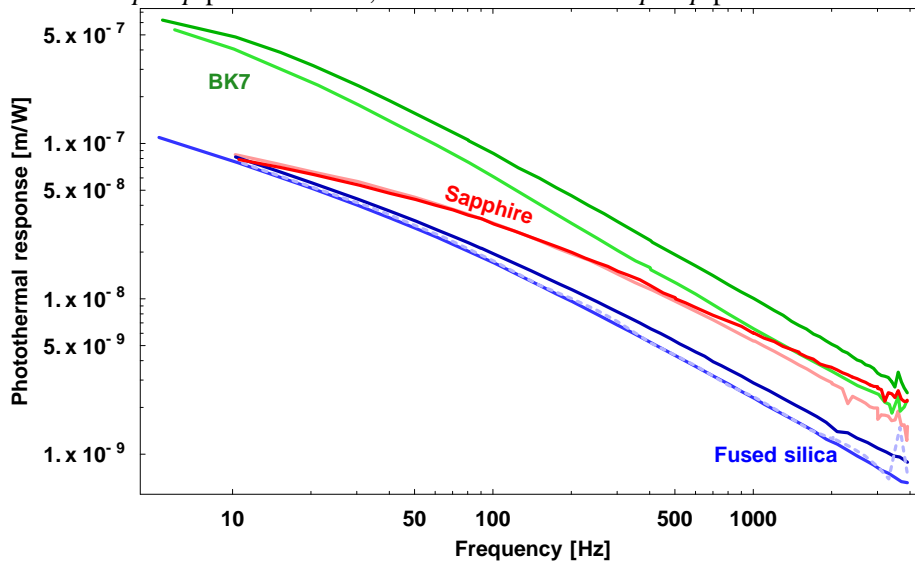


Figure 3.25: Ratio of photothermal displacement of samples with dielectric stacks to those without, normalized to 1 at 25 Hz. The ratios are based on linear interpolation between the measured data points, which are not always at the same frequencies. The data for BK7 are omitted above 3 kHz.

